$gg \to ZZ$: analytic two-loop results for the low- and high-energy regions

Joshua Davies[a], Go Mishima[a,b], Matthias Steinhauser[a], David Wellmann[a]

[a]*Institut für Theoretische Teilchenphysik*

Karlsruhe Institute of Technology (KIT)

Wolfgang-Gaede Straße 1, 76128 Karlsruhe, Germany

[b]*Institut für Kernphysik*

Karlsruhe Institute of Technology (KIT)

Hermann-von-Helmholtz-Platz 1, 76344 Eggenstein-Leopoldshafen, Germany

Abstract

We compute next-to-leading order virtual two-loop corrections to the process $gg \to ZZ$ in the low- and high-energy limits, considering the contributions with virtual top quarks. Analytic results for all 20 form factors are presented including expansion terms up to $1/m_t^{12}$ and m_t^{32}. We use a Padé approximation procedure to extend the radius of convergence of the high-energy expansion and apply this approach to the finite virtual next-to-leading order corrections.

1 Introduction

The production of Z boson pairs constitutes an important process at the CERN Large Hadron Collider (LHC). It can be measured with an accuracy of a few percent (see, e.g., Ref. [1, 2]) and, furthermore, plays an important role both for on-shell and off-shell Higgs boson production. The latter is particularly important in the context of the indirect determination of the Higgs boson width [3, 4], as was pointed out in Refs. [5–7].

In recent years there has been quite some activity on the theory side with the aim to compute higher order corrections which enable precise predictions. At tree level ZZ production proceeds via quark–anti-quark annihilation where NNLO corrections are available [8–14].

The gluon fusion channel is loop induced and is thus formally of NNLO. It turns out that the one-loop contribution [15] from massless quarks is quite large and amounts to more than half of the NNLO contribution [8]. NLO (two-loop) QCD corrections to $gg \to ZZ$ with massless quarks have been computed in Refs. [16, 17]. A large K-factor of 50-100% (depending of the renormalization and factorization scales) has been observed which increases the $pp \to ZZ$ cross section by about 5% [18].

The top quark contribution to $gg \to ZZ$ is expected to be particularly relevant for higher invariant masses providing a relevant impact on the indirect determination of the Higgs boson width [5–7]. Its computation is technically more challenging than the massless counterpart and currently only the one-loop corrections are available in exact form [15]. Exact two-loop corrections with virtual top quarks are not yet available, however, approximations have been considered by several groups. The leading term in the large top quark mass expansion has been considered in [19]. In Ref. [20] the interference of $gg \to ZZ$ with $gg \to H \to ZZ$ has been computed, in an expansion up to $1/m_t^{12}$. A conformal mapping and Padé approximation have been applied with the aim to extend the validity of the large-mass expansion. Furthermore, the (anomalous) double triangle contributions have been computed with exact dependence on the masses and kinematic variables. Recently, in Ref. [21] conformal mapping and Padé approximation have been used in order to combine information from the large-m_t and the threshold regions. Also in this work results are presented for the interference to the off-shell Higgs contributions.

In this work we concentrate on the loop-induced gluon fusion channel with virtual top quarks. Its leading (one-loop) term is already a NNLO contribution to $pp \to ZZ$. It amounts to a few percent of the numerically large massless contribution and it is thus desirable to compute the two-loop terms, which formally are N^{3}LO.

The contributing Feynman diagrams (see Fig. 1 for a few examples) can be subdivided into triangle and box contributions, where the former corresponds to $gg \to H \to ZZ$, i.e., a virtual Higgs boson connects the quark loop and the final-state Z boson. Exact results for the Higgs-gluon vertex corrections up to two loops are known from [22–24].

In this paper we compute analytic one- and two-loop results of the top quark contribution

2

for all 20 form factors. We choose an orthogonal basis which simplifies the computation of the squared amplitude. Expressing the final result as a linear combination of form factors provides full flexibility; for example, it is straightforward to compute the projection on the Higgs-induced sub-process $gg \to H \to ZZ$. In an alternative approach we also express our results in terms of helicity amplitudes (see, e.g., Ref. [16, 25]). We consider an expansion for both large and small top quark masses. In the latter case we take finite Z boson masses into account by a subsequent expansion in m_Z^2/m_t^2. Parts of our large-m_t results can be compared to Refs. [19, 20] whereas the high-energy results are new.

We do not consider the two-loop light-quark contributions, which are known from [16, 26]. Similarly, we do not consider the contribution originating from two quark triangles, which has been computed in [20]. We also do not compute real radiation contributions in this paper, but concentrate on the virtual corrections.

The remainder of the paper is organized as follows. In the next section we introduce our definitions and notation, and describe our methodology for the computation of the high-energy and large-m_t expansions. We also discuss how one can obtain helicity amplitudes from our form factors. In Section 3 we compare the expansions to the exact LO result and justify our choices for the expansion depths used at NLO. In Section 4 we describe how one can improve the radius of convergence of the high-energy expansions by making use of Padé approximants. Using this method, in Section 5 we show NLO results for form factors and for the finite virtual corrections to the cross section. For the latter, we consider different values for the transverse momentum of the Z bosons and demonstrate that we can obtain stable predictions for this quantity for transverse momentum values as small as 150 GeV. Our conclusions are presented in Section 6. In the Appendix we provide the explicit results for the relations which can be used to rotate to the orthogonal tensor basis of Section 2.3. Furthermore, numerical results for all LO and NLO form factors and analytic results for some example LO form factors are presented.

2 Technical details

In Fig. 1 we show one- and two-loop sample Feynman diagrams contributing to process

$$g(p_1)g(p_2) \to Z(p_3)Z(p_4) \,, \tag{1}$$

where all momenta p_i are incoming. The Mandelstam variables are defined as

$$
\begin{aligned}
s &= (p_1 + p_2)^2 \,, \\
t &= (p_1 + p_3)^2 \,, \\
u &= (p_1 + p_4)^2 \,,
\end{aligned}
\tag{2}
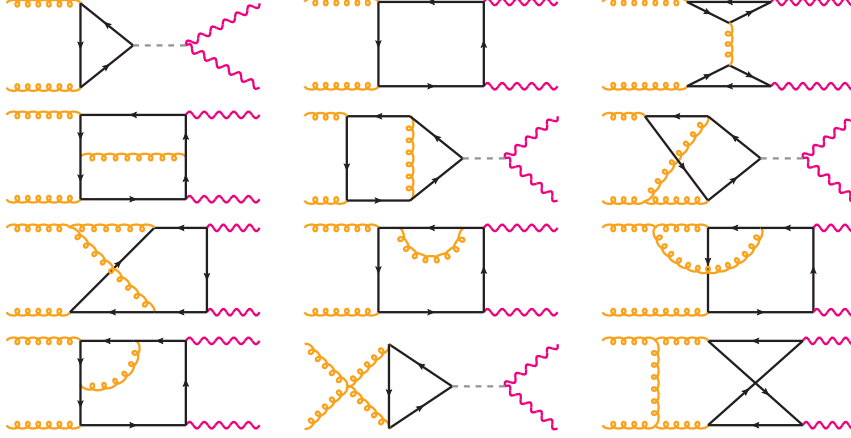$$

and fulfil the property

$$s + t + u = 2m_Z^2 \,. \tag{3}$$

Figure 1: Sample LO and NLO Feynman diagrams for $gg \to ZZ$. "Double triangle" diagrams (such as the third diagram) are known, and not considered here.

For later convenience we also introduce the velocity β and the transverse momentum of the Z bosons as

$$\beta = \sqrt{1 - \frac{4m_Z^2}{s}}\,, \qquad p_T = \sqrt{\frac{tu - m_Z^4}{s}} = \frac{\sqrt{s}}{2}\beta \sin\theta\,, \tag{4}$$

where θ is the scattering angle.

In this paper we consider only the top quark as the virtual particle in the loop. We exclude from our analysis the two-loop contribution which originates from the product of two one-loop triangle diagrams (the so-called anomaly contribution) since this contribution is discussed in detail in Ref. [20], in which exact results are presented.

The Z boson has a vector and axial-vector coupling to the top quark, for which the corresponding Feynman rule is given by

$$-i\frac{e}{2\sin\theta_W \cos\theta_W}\gamma^\mu\left(v_t + a_t\gamma_5\right)\,, \tag{5}$$

with

$$v_t = \frac{1}{2} - \frac{4}{3}\sin^2\theta_W\,, \qquad a_t = \frac{1}{2}\,. \tag{6}$$

θ_W denotes weak mixing angle and $e = \sqrt{4\pi\alpha}$ where α is the fine structure constant. The amplitude for $gg \to ZZ$ has contributions proportional to v_t^2 and a_t^2.

The polarization vectors of the gluons and Z bosons are given by $\varepsilon_{\lambda_1,\mu}(p_1)$, $\varepsilon_{\lambda_2,\nu}(p_2)$ and $\varepsilon_{\lambda_3,\rho}(p_3)$, $\varepsilon_{\lambda_4,\sigma}(p_4)$, in terms of which the amplitude can be written as

$$\mathcal{M}_{\lambda_1,\lambda_2,\lambda_3,\lambda_4} = A^{\mu\nu\rho\sigma}\varepsilon_{\lambda_1,\mu}(p_1)\varepsilon_{\lambda_2,\nu}(p_2)\varepsilon_{\lambda_3,\rho}(p_3)\varepsilon_{\lambda_4,\sigma}(p_4)\,. \tag{7}$$

4

Here the colour indices have been suppressed. $A^{\mu\nu\rho\sigma}$ is a linear combination of 20 tensor structures [16, 26, 27]

$$A^{\mu\nu\rho\sigma} = \sum_{i=1}^{20} f_i\, S_i^{\mu\nu\rho\sigma}, \tag{8}$$

where the tensor structures S_i are chosen as

$$
\begin{aligned}
&S_1^{\mu\nu\rho\sigma} = g^{\mu\nu}g^{\rho\sigma}, && S_2^{\mu\nu\rho\sigma} = g^{\mu\rho}g^{\nu\sigma}, && S_3^{\mu\nu\rho\sigma} = g^{\mu\sigma}g^{\nu\rho}, && S_4^{\mu\nu\rho\sigma} = g^{\mu\sigma}p_1^\rho p_3^\nu, \\
&S_5^{\mu\nu\rho\sigma} = g^{\mu\sigma}p_2^\rho p_3^\nu, && S_6^{\mu\nu\rho\sigma} = g^{\nu\sigma}p_1^\rho p_3^\mu, && S_7^{\mu\nu\rho\sigma} = g^{\nu\sigma}p_2^\rho p_3^\mu, && S_8^{\mu\nu\rho\sigma} = g^{\rho\sigma}p_3^\mu p_3^\nu, \\
&S_9^{\mu\nu\rho\sigma} = g^{\mu\nu}p_1^\rho p_1^\sigma, && S_{10}^{\mu\nu\rho\sigma} = g^{\mu\nu}p_1^\rho p_2^\sigma, && S_{11}^{\mu\nu\rho\sigma} = g^{\mu\nu}p_1^\sigma p_2^\rho, && S_{12}^{\mu\nu\rho\sigma} = g^{\mu\nu}p_2^\rho p_2^\sigma, \\
&S_{13}^{\mu\nu\rho\sigma} = g^{\mu\rho}p_1^\sigma p_3^\nu, && S_{14}^{\mu\nu\rho\sigma} = g^{\mu\rho}p_2^\sigma p_3^\nu, && S_{15}^{\mu\nu\rho\sigma} = g^{\nu\rho}p_1^\sigma p_3^\mu, && S_{16}^{\mu\nu\rho\sigma} = g^{\nu\rho}p_2^\sigma p_3^\mu, \\
&S_{17}^{\mu\nu\rho\sigma} = p_1^\rho p_1^\sigma p_3^\mu p_3^\nu, && S_{18}^{\mu\nu\rho\sigma} = p_1^\rho p_2^\sigma p_3^\mu p_3^\nu, && S_{19}^{\mu\nu\rho\sigma} = p_1^\sigma p_2^\rho p_3^\mu p_3^\nu, && S_{20}^{\mu\nu\rho\sigma} = p_2^\rho p_2^\sigma p_3^\mu p_3^\nu.
\end{aligned}
\tag{9}
$$

This set omits structures which would vanish after contraction with the following choice of polarization sums:

$$
\begin{aligned}
\sum_{\lambda_1} \varepsilon_{\lambda_1,\mu}(p_1)\varepsilon^*_{\lambda_1,\mu'}(p_1) &= -g_{\mu\mu'} + \frac{p_{1,\mu}p_{2,\mu'} + p_{2,\mu}p_{1,\mu'}}{p_1 \cdot p_2}, \\
\sum_{\lambda_2} \varepsilon_{\lambda_2,\nu}(p_2)\varepsilon^*_{\lambda_2,\nu'}(p_2) &= -g_{\nu\nu'} + \frac{p_{2,\nu}p_{1,\nu'} + p_{1,\nu}p_{2,\nu'}}{p_1 \cdot p_2}, \\
\sum_{\lambda_3} \varepsilon_{\lambda_3,\rho}(p_3)\varepsilon^*_{\lambda_3,\rho'}(p_3) &= -g_{\rho\rho'} + \frac{p_{3,\rho}p_{3,\rho'}}{m_Z^2}, \\
\sum_{\lambda_4} \varepsilon_{\lambda_4,\sigma}(p_4)\varepsilon^*_{\lambda_4,\sigma'}(p_4) &= -g_{\sigma\sigma'} + \frac{p_{4,\sigma}p_{4,\sigma'}}{m_Z^2}.
\end{aligned}
\tag{10}
$$

In order to obtain the scalar coefficients f_i we construct a projector for each S_i ($i = 1, \ldots, 20$); these are given as linear combinations of the 138 possible rank 4 tensor structures that can be constructed from the three independent four-vectors p_1, p_2, p_3, and the metric tensor. The scalar coefficients have a perturbative expansion in powers of the strong coupling constant which we write as

$$f_i = \delta_{ab}\frac{\sqrt{2}G_F m_Z^2 \alpha_s(\mu)}{\pi}\left[f_i^{(0)} + \frac{\alpha_s(\mu)}{\pi}f_i^{(1)} + \ldots\right], \tag{11}$$

where a and b are adjoint colour indices of the incoming gluons. The form factors $f_i^{(0)}$ and $f_i^{(1)}$ can be separated into triangle and box contributions

$$f_i^{(j)} = \frac{s}{3(s - m_H^2)}f_{i,\text{tri}}^{(j)} + f_{i,\text{box}}^{(j),v_t} + f_{i,\text{box}}^{(j),a_t} \tag{12}$$

where the superscripts "v_t" and "a_t" refer to the contributions proportional to v_t^2 and a_t^2, respectively. $f_{i,\text{tri}}^{(j)}$ describes contributions from diagrams which contain a Higgs-ZZ

coupling, and we note that only $f_{1,\text{tri}}^{(j)}$ is non-zero. In the case of massless quark loops, $f_{i,\text{box}}^{(j),v_t}/v_t^2 = f_{i,\text{box}}^{(j),a_t}/a_t^2$ [15]. This property is satisfied by the leading term of our high-energy expansions ($m_t^0 m_Z^0$) but is violated in higher order terms, including for higher order terms in m_Z since $m_Z < m_t$.

These form factors are, at this point, divergent in 4 dimensions. We perform the renormalization of the top quark mass, the strong coupling constant and the gluon field to remove the ultra-violet divergences. The remaining divergences are infrared in nature and are removed by the subtraction procedure of Ref. [28], which we outline here.

We construct finite form factors which are defined as

$$f_i^{(1),\text{fin}} = f_i^{(1),\text{IR}} - K_g^{(1)} f_i^{(0)} , \tag{13}$$

where $f^{(1),\text{IR}}$ is ultraviolet renormalized but still infrared divergent. $K_g^{(1)}$ can be found in Ref. [28] and is given by

$$K_g^{(1)} = -\left(\frac{\mu^2}{-s-i\delta}\right)^\epsilon \frac{e^{\epsilon\gamma_E}}{2\Gamma(1-\epsilon)} \left[\frac{C_A}{\epsilon^2} + \frac{2\beta_0}{\epsilon}\right] , \tag{14}$$

where γ_E is Euler's constant. Note that the poles in the terms proportional to n_f from Eq. (14) cancel against the counterterm contribution induced by the α_s renormalization. However, finite terms proportional to $\log(\mu^2/(-s-i\delta))$ remain, which can be cast in the form

$$f_i^{(1),\text{fin}} = \tilde{f}_i^{(1)} + \beta_0 \log\left(\frac{\mu^2}{-s-i\delta}\right) f_i^{(0)} , \tag{15}$$

with $\beta_0 = 11C_A/12 - Tn_f/3$. Only $\tilde{f}_i^{(1)} \equiv f_i^{(1),\text{fin}}(\mu^2 = -s)$, which are independent of μ, contain new information and thus only they will be discussed in Section 5.

We now discuss the work-flow for our calculation of these form factors, as expansions in both the high-energy (Section 2.1) and large-m_t (Section 2.2) limits. Analytic expressions for the results of both of these expansions can be found in the ancillary file of this paper [29]. In both cases, the amplitude is generated using qgraf [30]. Each Feynman diagram is then contracted with one of the 138 possible tensor structures discussed above, as a separate computation. This splitting is particularly important for the large-m_t expansion of Section 2.2, in order to avoid overly large intermediate expressions.

We additionally reproduce the exact LO result from [15] using the programs FeynArts 3.10 [31] and FormCalc 9.8 [32]. The scalar Passarino-Veltman functions B_0, C_0 and D_0 are rewritten in terms of polylogarithms with the help of Package-X [33], which allows for a high-precision evaluation within Mathematica. We use this exact LO result to evaluate the performance of our expansions and approximation methods in Section 3.

6

2.1   High-energy expansion

For each contraction we compute the fermion traces and write the result in terms of scalar Feynman integrals, belonging to one of the integral families defined in Refs. [34,35] (there in the context of an NLO calculation of $gg \to HH$ in the high-energy limit). We then construct the appropriate linear combinations which are required to obtain the form factors of the 20 tensor structures given in Eq. (9). Up to this point our calculation is exact in all kinematic variables and masses.

Next, we Taylor expand both the scalar Feynman integrals and their coefficients in m_Z, using the program `LiteRed` [36] and in-house `FORM` [37] routines. For each integral family we perform an integration-by-parts (IBP) reduction to master integrals using version 6 of `FIRE` [38] and symmetry relations obtained using `LiteRed` [36]. Since we have performed a Taylor expansion the integrals depend on the kinematic variables and m_t, but no longer on m_Z; this makes the IBP reduction much more tractable. For the most complicated family (numbered 91 in Appendix A of Ref. [35]) this takes about 4.5 days[1] on a 3.5 GHz machine with 32 cores.

Inserting the reduction tables into the amplitude and expanding the resulting expressions in m_t and ϵ took around three weeks on a reasonably sized cluster of computers. Using the results for the master integrals of Refs. [34,35], we produce an expression for the amplitude expanded up to m_t^{32} and m_Z^4. The coefficients of the expansion terms are functions of s and t, and are written in terms of Harmonic Polylogarithms with a harmonic weight of at most 4, for the numerical evaluation of which we use the package `HPL.m` [39].

The expansions contain terms with both even and odd powers of m_t; the odd powers come from the expansions of the two-loop non-planar master integrals. Most of the odd powers cancel in the amplitude, however starting from m_t^3, odd m_t powers remain in the imaginary part of the non-abelian contribution to the form factors. The situation is analogous to $gg \to HH$ [35] where the contributions of odd powers is discussed in detail at the level of master integrals.

2.2   Large-m_t expansion

We keep the discussion of the large-m_t expansion brief, since the methods are largely the same as used in the expansion of Higgs boson pair production, described in detail in Ref. [40]. At the level of the individual Feynman diagrams contracted with one of the 138 possible tensor structures, we apply an asymptotic expansion for $m_t \gg p_1, p_2, p_3$ using the program `exp` [41, 42].

This leads to one- and two-loop vacuum integrals with the scale m_t multiplied by massless three-point integrals with the scale s. We expand, at one and two loops, to order $1/m_t^{12}$.

---

[1]We note that here we reduce a factor of 4 more integrals compared to Refs. [34,35]. Nevertheless, the reductions take a similar amount of CPU time due to the performance improvements of `FIRE 6` compared to `FIRE 5.2`.

After expansion, we compute the appropriate linear combinations of the contractions in order to arrive at the coefficients of the 20 tensor structures of Eq. (8), yielding the large-m_t expanded expressions for the form factors defined in Eq. (12). For the convenience of the reader we show the leading terms in the $1/m_t$ expansion for some form factors in Appendix D.

In Ref. [19] the amplitude for $gg \to ZZ$ has been calculated at LO and NLO up to the first non-vanishing expansion term in $1/m_t$, which only involves the axial-vector part. We find agreement after fixing two obvious typos[2]. Furthermore, in Ref. [20] analytic results for the $gg \to ZZ$ amplitude projected to the triangle contribution are presented as an expansion up to order $1/m_t^{12}$. After performing the same projection we could successfully compare our results for the vector and axial-vector part which constitutes a welcome check for our approach.

2.3 Orthogonal tensor basis

The tensors given in Eq. (9) have the advantage of being simple and compact. However, they are not orthogonal; this leads to non-vanishing cross terms when squaring the amplitude. For this reason we construct a new basis T_i, using the Gram-Schmidt orthogonalization procedure, which has the property

$$c_i \delta_{ij} \overset{d \to 4}{=} \sum_{\lambda_1, \lambda_2, \lambda_3, \lambda_4} T_i^{\mu \nu \rho \sigma} T_j^{*, \mu' \nu' \rho' \sigma'} \times$$

$$\varepsilon_{\lambda_1, \mu}(p_1) \varepsilon_{\lambda_2, \nu}(p_2) \varepsilon_{\lambda_3, \rho}(p_3) \varepsilon_{\lambda_4, \sigma}(p_4) \varepsilon_{\lambda_1, \mu'}^*(p_1) \varepsilon_{\lambda_2, \nu'}^*(p_2) \varepsilon_{\lambda_3, \rho'}^*(p_3) \varepsilon_{\lambda_4, \sigma'}^*(p_4) \qquad (16)$$

For $d = 4$ the coefficients c_i are given by

$$c_1 = c_2 = \cdots = c_{10} = 1 \quad , \quad c_{11} = c_{12} = \cdots = c_{18} = p_T^2 m_Z^2 \quad , \quad c_{19} = c_{20} = 0 \ . \qquad (17)$$

Note that in four dimensions c_{19} and c_{20} vanish which means that in the orthogonal basis only 18 form factors contribute to the final results. To obtain Eq. (17) we have made use of the polarization sums already listed in Eq. (10).

The basis change from S_i to T_i is described in Appendix A. In terms of T_i the amplitude in Eq. (8) reads

$$A^{\mu \nu \rho \sigma} = \sum_{i=1}^{18} F_i \frac{T_i^{\mu \nu \rho \sigma}}{\sqrt{c_i}} \ . \qquad (18)$$

where the factors $1/\sqrt{c_i}$ have been introduced such that the coefficients F_i are dimensionless. As for f_i, the coefficients F_i have a decomposition into form factors $F_{i,\mathrm{tri}}^{(j)}$, $F_{i,\mathrm{box}}^{(j), v_t}$

---

[2]In Eq. (5) of [19] the term $f_{\mu \rho}^1 f_\beta^{2,\mu}$ should be multiplied by (-1) and in Eq. (7) p_1^μ and p_2^ν should be replaced by p_2^μ and p_1^ν, respectively.

and $F_{i,\text{box}}^{(j),a_t}$ as described in Eq. (12). It is in terms of these form factors, of the orthogonal basis of tensor structures, that we write an expression for the differential cross section:

$$\frac{d\sigma}{dt} = \frac{G_F^2 m_Z^4}{512\pi s^2} \left(\frac{\alpha_s}{\pi}\right)^2 \sum_{i=1}^{18} \left[\left|F_i^{(0)}\right|^2 + \frac{\alpha_s}{\pi}\left(F_i^{(0)*} F_i^{(1),\text{fin}} + F_i^{(0)} F_i^{(1),\text{fin}*} + R\right)\right], \quad (19)$$

where "R" denotes the corrections due to real radiation which we do not consider here. The basis change is computed numerically, upon evaluation of the differential cross section for particular values of the kinematic parameters.

2.4 Helicity amplitudes

In this subsection we describe how one can obtain the helicity amplitudes for the process $gg \to ZZ$ from the tensor decomposition which we have introduced above. For this purpose it is convenient to explicitly specify the external momenta and to introduce polarization vectors as follows:[3]

$$p_1 = \frac{\sqrt{s}}{2}\begin{pmatrix} 1 \\ 0 \\ 0 \\ 1 \end{pmatrix}, \quad p_2 = \frac{\sqrt{s}}{2}\begin{pmatrix} 1 \\ 0 \\ 0 \\ -1 \end{pmatrix}, \quad p_3 = \frac{\sqrt{s}}{2}\begin{pmatrix} -1 \\ -\beta\sin\theta \\ 0 \\ \beta\cos\theta \end{pmatrix}, \quad p_4 = \frac{\sqrt{s}}{2}\begin{pmatrix} -1 \\ \beta\sin\theta \\ 0 \\ -\beta\cos\theta \end{pmatrix},$$

$$\varepsilon_+(p_1) = \varepsilon_-(p_2) = [\varepsilon_-(p_1)]^* = [\varepsilon_+(p_2)]^* = \frac{1}{\sqrt{2}}\begin{pmatrix} 0 \\ i \\ 1 \\ 0 \end{pmatrix}, \quad \varepsilon_0(p_3) = \frac{\sqrt{s}}{2m_Z}\begin{pmatrix} \beta \\ -\sin\theta \\ 0 \\ -\cos\theta \end{pmatrix},$$

$$\varepsilon_+(p_3) = \varepsilon_-(p_4) = [\varepsilon_-(p_3)]^* = [\varepsilon_+(p_4)]^* = \frac{1}{\sqrt{2}}\begin{pmatrix} 0 \\ i\cos\theta \\ 1 \\ i\sin\theta \end{pmatrix}, \quad \varepsilon_0(p_4) = \varepsilon_0(p_3)\Big|_{\theta\to\theta+\pi}, \quad (20)$$

where ε_0 denotes the longitudinal components of polarization vectors. Recall that all external momenta are defined as incoming and that the polarization vectors are chosen such that they satisfy Eq. (10). The helicity amplitudes $\mathcal{M}_{\lambda_1,\lambda_2,\lambda_3,\lambda_4}$ are given by Eq. (7). In total there are $2 \times 2 \times 3 \times 3 = 36$ helicity amplitudes. However, due to various symmetries only eight of them are independent. First, due to

$$[p' \cdot \varepsilon_\pm(p)]^* = p' \cdot \varepsilon_\mp(p), \quad (21)$$

which holds for $p, p' = p_1, ..., p_4$, we have

$$\left|\mathcal{M}_{-\lambda_1,-\lambda_2,-\lambda_3,-\lambda_4}\right| = \left|\mathcal{M}_{\lambda_1,\lambda_2,\lambda_3,\lambda_4}\right|, \quad (22)$$

---

[3]Alternatively one can introduce the so-called spinor-helicity notation, see, e.g., Refs. [16, 25].

which reduces the number of independent amplitudes to 18. Furthermore, there are additional symmetries [15] relating helicity amplitudes with different polarization states

$$
\begin{aligned}
\mathcal{M}_{+++-} &= \mathcal{M}_{++-+}\,, \\
\mathcal{M}_{+---} &= \mathcal{M}_{+-++}\,, \\
\mathcal{M}_{++\pm 0} &= \mathcal{M}_{++0\pm}\,, \\
\mathcal{M}_{+-\pm 0} &= -\mathcal{M}_{+-0\mp}\,,
\end{aligned}
\tag{23}
$$

and there are symmetry relations due to $\beta \to -\beta$,

$$
\begin{aligned}
\mathcal{M}_{++--} &= \mathcal{M}_{++++}\big|_{\beta \to -\beta}\,, \\
\mathcal{M}_{+--+} &= \mathcal{M}_{+-+-}\big|_{\beta \to -\beta}\,, \\
\mathcal{M}_{+\pm +0} &= \mathcal{M}_{+\pm -0}\big|_{\beta \to -\beta}\,.
\end{aligned}
\tag{24}
$$

Note that this replacement changes none of the Mandelstam variables s, t, u. Using Eqs. (23) and (24) reduces the number of independent helicity amplitudes by six and four, respectively, and we arrive at eight independent helicity amplitudes.

It turns out that the above symmetries are fulfilled when the form factors satisfies the relations

$$
f_{12} = f_9\,, \quad f_{20} = f_{17}\,, \quad f_{16} = -f_4\,, \quad f_{15} = -f_5\,, \quad f_{14} = -f_6\,, \quad f_{13} = -f_7\,.
\tag{25}
$$

Note that up to this point we do not make use of any approximation. We use the relations (25) as a cross check of our calculations.

The LO results for the eight independent helicity amplitudes are provided in Ref. [15] and we confirm the agreement between them and our results.[4] For the results of the high-energy expansion we have expanded in m_Z, making the symmetry relations due to $\beta \to -\beta$ hard to realize, since $\beta = 1 - 2m_Z^2/s + \mathcal{O}(m_Z^4)$ and we do not distinguish the origin of m_Z terms in the expression. For this reason, in the ancillary file [29] we provide results for the twelve helicity amplitudes

$$
\begin{aligned}
&\mathcal{M}_{++++}\,, \quad \mathcal{M}_{++--}\,, \quad \mathcal{M}_{+-+-}\,, \\
&\mathcal{M}_{+--+}\,, \quad \mathcal{M}_{+++0}\,, \quad \mathcal{M}_{++-0}\,, \\
&\mathcal{M}_{+-+0}\,, \quad \mathcal{M}_{+--0}\,, \quad \mathcal{M}_{+++-}\,, \\
&\mathcal{M}_{++00}\,, \quad \mathcal{M}_{+-++}\,, \quad \mathcal{M}_{+-00}\,.
\end{aligned}
\tag{26}
$$

---

[4] Note that in Ref. [15] one has to replace the D-functions (but not the B- or C-functions) with $D \to i\pi^2 D$ in order to obtain the correct results. Additionally, a factor $1/3$ is missing for the contributions from the triangle diagrams in the large-m_t limit.

3 Comparison at leading order

This section is devoted to the discussion of the LO contribution to $gg \to ZZ$ with virtual top quarks. We first consider the form factors and helicity amplitudes, and compare the large-m_t and high-energy expansions with the exact results. Afterwards we discuss our approach to improve the radius of convergence of our expansions, which is based on Padé approximations. We furthermore investigate the importance of finite Z boson mass corrections. For the numerical evaluation we use the following input values [43]

$$
\begin{aligned}
G_F &= 1.1663787 \times 10^{-5} \text{ GeV}^{-2} \,, \\
\sin^2 \theta_W &= 0.23122 \,, \\
\alpha_s(m_Z) &= 0.1181 \,, \\
m_Z &= 91.1876 \text{ GeV} \,, \\
m_H &= 125.10 \text{ GeV} \,, \\
m_t &= 172.9 \text{ GeV} \,.
\end{aligned}
\tag{27}
$$

As typical examples for the LO form factors, in Fig. 2 we show the results for $F_1^{(0)}$ and $F_{16}^{(0)}$ as a function of the partonic center-of-mass energy $\sqrt{s}$. For the scattering angle we choose $\theta = \pi/2$. The solid blue and purple lines correspond to the real and imaginary parts of the exact result. The dotted curve includes seven terms (up to $1/m_t^{12}$) in the large-m_t expansion and agrees with the blue curve almost up to the top quark threshold at $\sqrt{s} \approx 2m_t$. The dash-dotted lines correspond to the high-energy expansion. Both for the real and imaginary parts we plot the expansions including terms up to m_t^{30} and m_t^{32}. One observes that they start to deviate from the exact result around the same value of $\sqrt{s}$. In fact, in these plots it is sufficient to include expansion terms only up to m_t^{16} to have a very similar high-energy approximation. Thus, the high-energy expansions
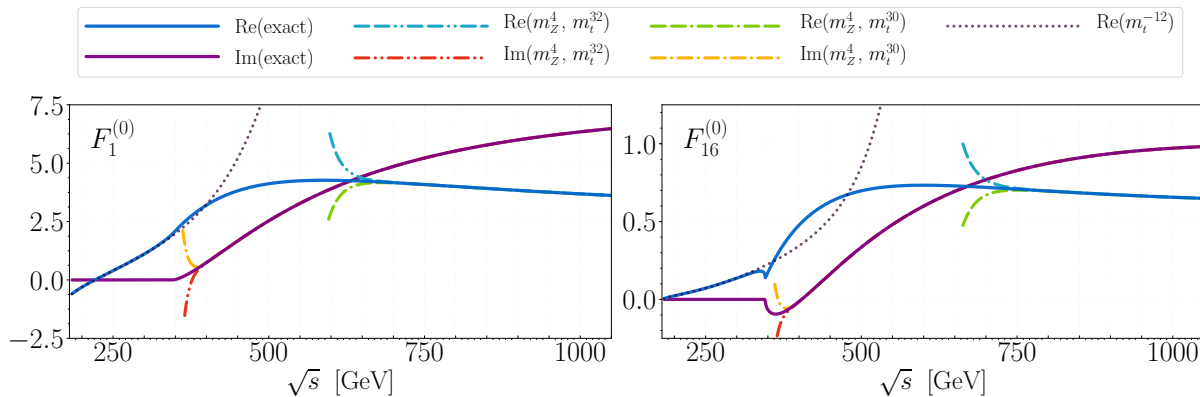

Figure 2: The LO form factors of the tensor structure T_1 and T_{16} as a function of $\sqrt{s}$, plotted for $\theta = \pi/2$. Both the real and imaginary parts are shown. Solid, dash-dotted and dotted lines correspond to the exact, high-energy and large-m_t results.
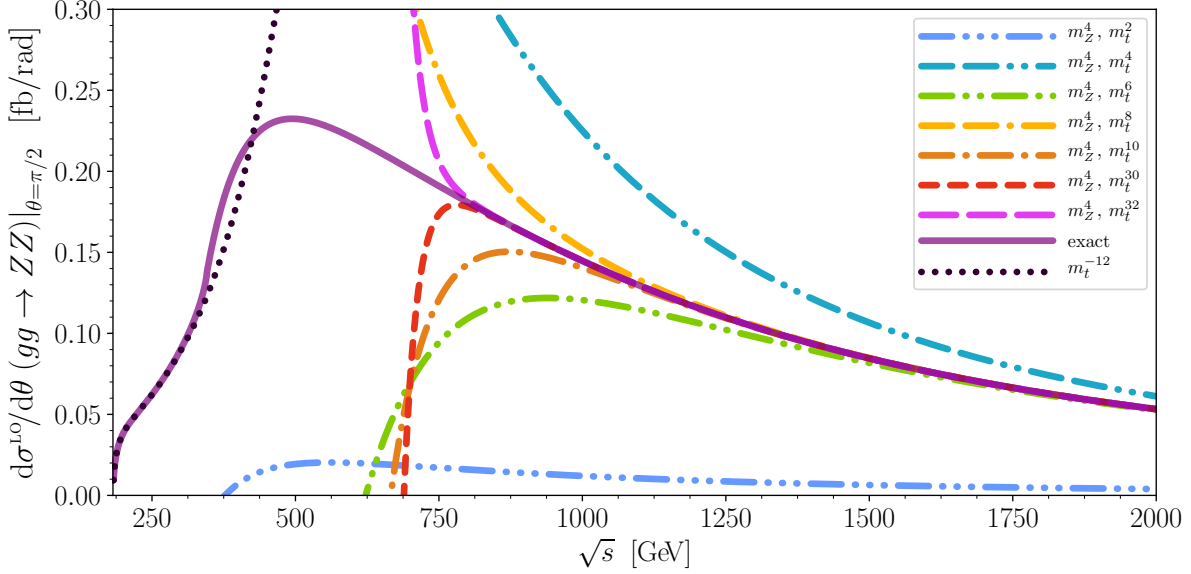
Figure 3: LO partonic differential cross section for $gg \to ZZ$ for $\theta = \pi/2$. Solid, dash-dotted and dotted lines correspond to the exact, high-energy and large-m_t results.

approximate the exact curves well for $\sqrt{s}$ values above about 750 GeV and 400 GeV for the real and imaginary parts, respectively. Similar plots for all 20 form factors are shown in Appendix B.

Fig. 3 shows (again for $\theta = \pi/2$) the LO partonic cross section as a function of $\sqrt{s}$. For low values of $\sqrt{s}$ we observe that the large-m_t result (dotted) approximates the exact curve (solid) well, almost up to the top quark threshold. The remaining curves (dashed and dash-dotted) incorporate results from the high-energy expansion. We show a selection of expansion depths between m_t^2 and m_t^{32}. One observes that five to six expansion terms are necessary in order to obtain a good approximation of the exact result for $\sqrt{s} \gtrsim 1000$ GeV. The deeper expansion depths show agreement down to $\sqrt{s} \approx 750$ GeV, which cannot be further improved even by including terms up to m_t^{32}. It appears that the simple expansions in m_t^2/s, m_t^2/t and m_t^2/u have a finite radius of convergence, which for $\theta = \pi/2$ manifests itself around $\sqrt{s} \approx 750$ GeV. This feature can be understood by inspecting the functions which are present in the exact one-loop result. Among others we have identified logarithms and di-logarithms which depend on the quantity

$$X = \sqrt{1 + \frac{4sm_t^2}{ut - m_Z^4}} = \sqrt{1 + \frac{4sm_t^2}{ut}} + \mathcal{O}\left(m_Z^4\right) \tag{28}$$

which has, in the high-energy limit, a radius of convergence of $ut/s = 4m_t^2$. For $\theta = \pi/2$ we have $t = u = -s/2$ which leads to $\sqrt{s} = 4m_t \simeq 700$ GeV.

Let us next discuss the importance of finite m_Z terms. The high-energy approximations shown in Figs. 2 and 3 include terms up to order m_Z^4, i.e., three expansion terms. In Fig. 4
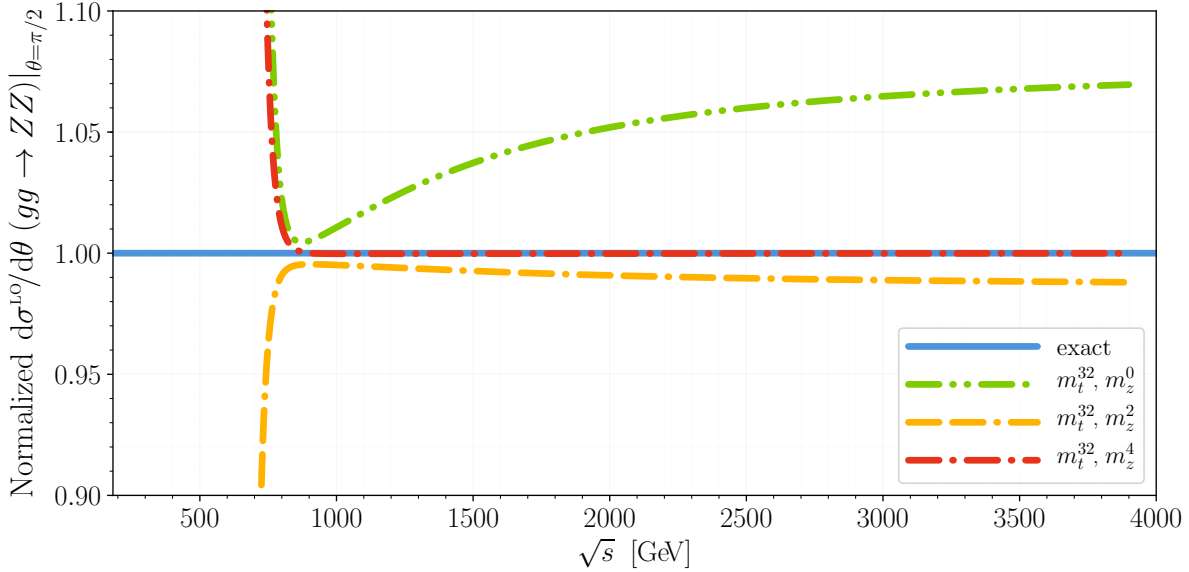
12

Figure 4: LO partonic differential cross section for $gg \to ZZ$ for $\theta = \pi/2$, normalized to the exact result. The three high-energy expansions contain terms up to order m_t^{32} and m_Z^0, m_Z^2 and m_Z^4.

we show how the number of expansion terms in m_Z^4 affects the quality of the expansion of the LO differential cross section. Curves including terms to m_t^{32} and m_Z^0, m_Z^2 and m_Z^4 are shown, normalized to the exact result. For all three curves we observe, as discussed above, a divergent behaviour for $\sqrt{s} \lesssim 750$ GeV. The m_Z^0 curve shows a more than 5% deviation from the exact result and including the m_Z^2 term leads to a significant improvement, with the deviation reducing to around 1%. Finally, including the m_Z^4 term produces a per-mille level agreement with the exact result, which motivates our computation of the m_Z^4 expansion terms of the NLO quantities discussed in later sections of this paper.

4   Padé-improvement of the high energy expansion

In Section 3 we investigated the behaviour of the expansions and, in particular, noted that the high-energy expansion fails to converge below $\sqrt{s} \approx 750$GeV regardless of how many expansion terms are included. In this section we discuss a method by which we can extend the prediction of the high-energy expansion to smaller values of $\sqrt{s}$.

The method is an extended version of the approach used in Ref. [44] in the context of Higgs boson pair production, and we describe it in detail below. It is based on the construction of a number of Padé approximants using the terms of the high-energy expansion, and subsequently combining the approximants to produce a central value and uncertainty estimate for a given phase-space point $\{\sqrt{s}, p_T\}$. We describe the procedure in terms of a

generic quantity $\mathcal{F}$ for which we assume an expansion in m_t is available. $\mathcal{F}$ also depends on the kinematic quantities s and p_T and on m_Z. In our practical applications $\mathcal{F}$ can be either a form factor, a helicity amplitude or the virtual finite cross section defined in Section 5.

The approximation procedure for $\mathcal{F}$ is then as follows:

- We write $\mathcal{F}$ as an expansion in m_t and define

$$\mathcal{F}^N = \mathcal{F}_0 + \sum_{i=2}^{N} \mathcal{F}_i \, m_t^i \,, \tag{29}$$

  where $\mathcal{F}_0$ contains the exact (in m_t and m_Z) expressions of the LO contributions. $\mathcal{F}_i$ are the m_t expansion coefficients.

- We apply the replacements $m_t^{2k} \to m_t^{2k} x^k$ and $m_t^{2k-1} \to m_t^{2k-1} x^k$ for the odd and even powers of m_t. We insert numerical values for m_t, m_Z, s and p_T, yielding a polynomial in the variable x.

- Next we construct Padé approximants of $\mathcal{F}^N$ in the variable x and write $\mathcal{F}^N$ as a rational function of the form

$$\mathcal{F}^N = \frac{a_0 + a_1 x + \ldots + a_n x^n}{1 + b_1 x + \ldots + b_m x^m} \equiv [n/m](x) \,. \tag{30}$$

  The coefficients a_i and b_i are determined by comparing the coefficients of x^k after expanding the right-hand side of Eq. (30) around the point $x = 0$. Evaluation of this rational function at $x = 1$ yields the Padé approximated value of $\mathcal{F}^N$.

The numerator and denominator degrees in Eq. (30) are free parameters; one only must ensure that $n + m \leq N/2$ such that a sufficient number of expansions terms are available to determine the coefficients a_i and b_i. We construct many Padé approximations and combine them to obtain a prediction for the central value and the uncertainty of $\mathcal{F}$.

The rational function of Eq. (30) develops poles which, for some Padé approximants, might lie close to the evaluation point $x = 1$ and yield unphysical results. In the following we describe a weighting scheme which minimizes the influence of such Padé approximants. We call this approach a *pole distance reweighted* (PDR) Padé approximation.

- For each phase-space point $\{\sqrt{s}, p_T\}$ we compute, for each Padé approximant, the value at $x = 1$ and the distance of the nearest pole which we denote by α_i and β_i, respectively.

- Introduce a weighting function, which reduces the impact of values α_i from Padé approximations with poles close to $x = 1$. We define

$$\omega_{i,\text{poles}} = \frac{\beta_i^2}{\sum_j \beta_j^2} \,, \tag{31}$$

  where the sum runs over all Padé approximants under consideration.

14

- Use the values α_i and $\omega_{i,\text{poles}}$ to compute the weighted average and weighted standard deviation of the Padé approximants,

$$\alpha = \sum_i \omega_{i,\text{poles}} \alpha_i \,, \qquad \delta_\alpha = \sqrt{\frac{\sum_i \omega_{i,\text{poles}} \left(\alpha_i - \alpha\right)^2}{1 - \sum_i \omega_{i,\text{poles}}^2}} \,. \tag{32}$$

These form the central value and error estimate of the approximation.

At this point, the procedure is the same as that of Ref. [44], in which expansions up to m_t^{30} and m_t^{32} were used to create Padé approximants with $15 \leq n + m \leq 16$, with the additional restriction to "near-diagonal" approximants which satisfy $|n - m| \leq 2$. This results in 5 possible approximants,

$$\{[7/8], [8/7], [7/9], [8/8], [9/7]\} \,, \tag{33}$$

which were weighted according to the above procedure to produce a central value and error estimate.

In this paper we further refine the method which allows us to loosen the restrictions and thus include more approximants in the computation. We introduce two additional weights into the averaging procedure which a) emphasize the contribution from Padé approximants which are derived from a larger number of expansion terms and b) emphasize the contribution from "near-diagonal" approximants. These weights are defined as follows:

a). An $[n_i/m_i]$ Padé approximant is weighted by

$$\omega_{i,\text{input}} = \frac{(n_i + m_i)^2}{\sum_j (n_j + m_j)^2} \,. \tag{34}$$

b). An $[n_i/m_i]$ Padé approximant is also weighted by

$$\omega_{i,\text{diag}} = \frac{|n_i - m_i|^2}{\sum_j |n_j - m_j|^2} \,. \tag{35}$$

As above, the sums run over all Padé approximants under consideration. The weights of Eqs. (31), (34) and (35) are combined according to

$$\omega_i = \frac{\left[\omega_{i,\text{poles}} \cdot \omega_{i,\text{input}} \cdot \left(1 - \omega_{i,\text{diag}}\right)\right]^2}{\sum_j \left[\omega_{j,\text{poles}} \cdot \omega_{j,\text{input}} \cdot \left(1 - \omega_{j,\text{diag}}\right)\right]^2} \,, \tag{36}$$

and used to form a central value and error estimate

$$\alpha = \sum_i \omega_i \alpha_i \,, \qquad \delta_\alpha = \sqrt{\frac{\sum_i \omega_i \left(\alpha_i - \alpha\right)^2}{1 - \sum_i \omega_i^2}} \,. \tag{37}$$

15

The approximation of Eq. (32) used in Ref. [44], with the restrictions described above, can be considered to be a special case of the same procedure with the weights of Eqs. (34) and (35) replaced with step functions. In this refined procedure we include a wider set of Padé approximants. We define the quantities N_{low} and N_{high} such that

$$N_{\text{low}} \leq n + m \leq N_{\text{high}} \quad \text{and} \quad N_{\text{low}} \leq n + m - |n - m|. \tag{38}$$

In Section 5 we will study the quality of the approximations due to the choices of $\{N_{\text{low}}, N_{\text{high}}\} = \{10, 16\}, \{9, 13\}, \{7, 11\}$ and $\{5, 9\}$. The best approximation is given by $\{10, 16\}$ which contains the following Padé approximants,

$$\Big\{ [5/5], [5/6], [6/5], [5/7], [7/5], [6/6], [5/8], [8/5], [6/7], [7/6], [5/9], [9/5], [6/8], [8/6], [7/7], $$
$$[5/10], [10/5], [6/9], [9/6], [5/11], [11/5], [7/8], [8/7], [6/10], [10/6], [7/9], [9/7], [8/8] \Big\},$$

a much larger number compared to the method of Ref. [44], listed in Eq. (33).

In Fig. 5 we demonstrate the effect of including higher order terms in the expansion in m_Z in the construction of the Padé approximants for the LO differential cross section $d\sigma/d\theta$. We show plots for $p_T = 150$ GeV and $p_T = 200$ GeV and, from top to bottom, approximations formed from high-energy expansions which include m_Z^0, m_Z^2 and m_Z^4 terms. One observes that it is crucial to include corrections at least to order m_Z^2, and that the results are further improved by including additionally the m_Z^4 terms. These improvements are in line with the expectations due to the behaviour of the high-energy expansion as demonstrated in Fig. 4. We note that in the $p_T = 200$ GeV plots, the majority of the points have error bars which are too small to be visible. After including the higher order m_Z terms, the exact results lie within the error estimates of the approximations, demonstrating that they are realistic.

The bottom-left plot of Fig. 5 we additionally show, in black, a Padé approximation according to the simpler prescription of Eq. (32) using the five Padé approximants of the set Eq. (33). One observes that for small values of $\sqrt{s}$ the exact result lies outside of the error estimates and that for large values of $\sqrt{s}$ the errors appear to be overestimated. In our view the purple points provide a more reasonable description of the uncertainty.

It is interesting to have a closer look at the effective expansion parameters entering the high-energy expansion; the final result is expressed as an expansion in m_t^2/s, m_t^2/t and m_t^2/u. Fig. 5 shows that the Padé-improved approximations reproduce the exact result for rather low values of p_T and $\sqrt{s}$, such as $\{p_T, \sqrt{s}\} = \{200, 450\}$ GeV or $\{p_T, \sqrt{s}\} = \{150, 500\}$. For these points, the expansion parameters $\{m_t^2/s, m_t^2/t, m_t^2/u\}$ have the values $\{0.15, -0.42, -0.26\}$ and $\{0.12, -1.08, -0.14\}$. In both cases one parameter becomes large or even exceeds 1, however the Padé approximants nonetheless produce reliable results.
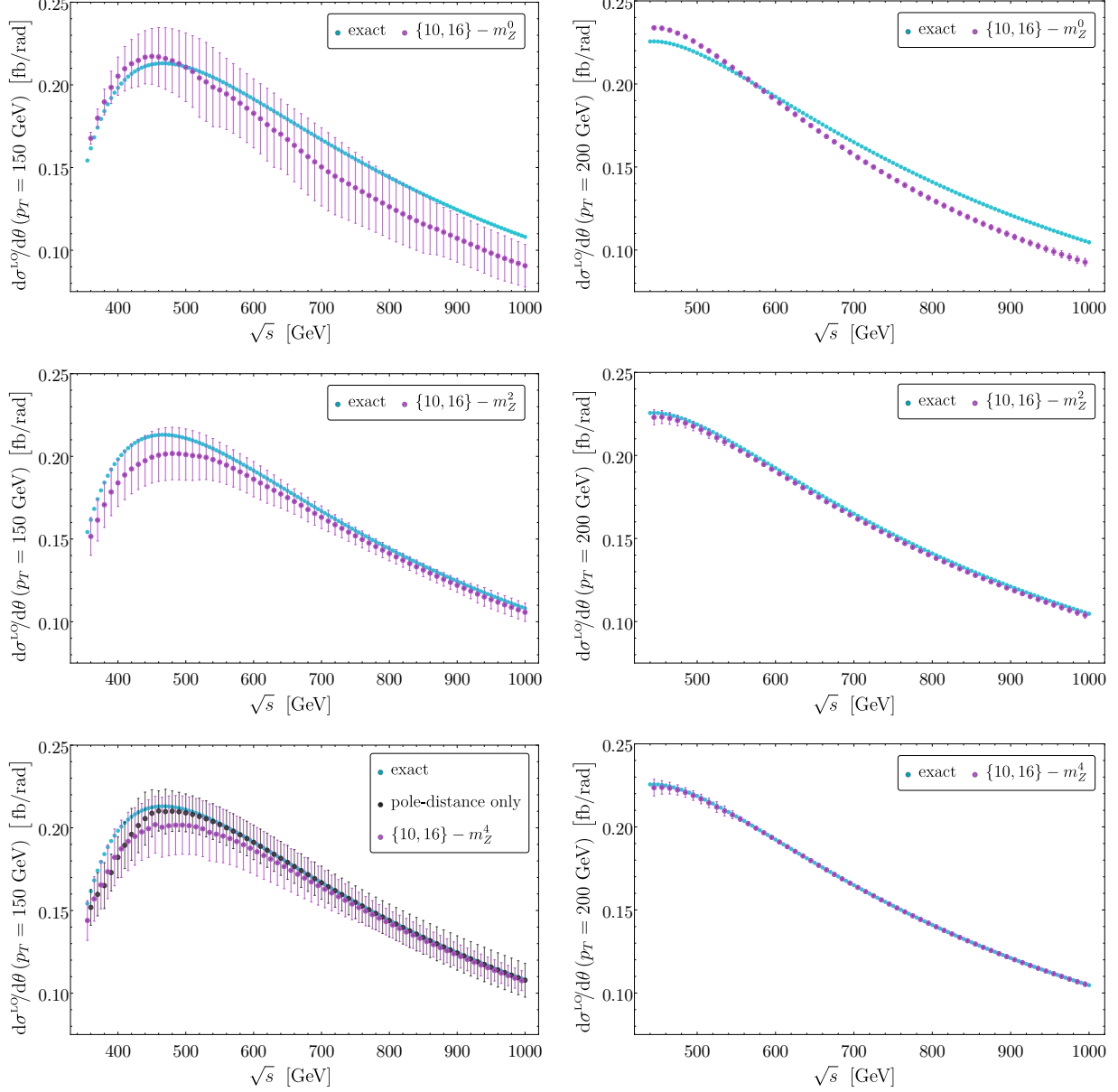
Figure 5: LO partonic differential cross section for $gg \to ZZ$ for $p_T = 150$ GeV (left column) and $p_T = 200$ GeV (right column) as a function of $\sqrt{s}$. The blue points are the exact result, and the purple points are the central values with uncertainties according to the prescription of Eq. (37). The bottom left plot shows additionally central values and uncertainties according to Eq. (32). The first, second and third rows show Padé approximants constructed from expansions including terms to m_Z^0, m_Z^2 and m_Z^4, respectively.

5 NLO results for $gg \to ZZ$ with virtual top quarks

In this Section we apply the approximation procedure of Section 4 to our results for NLO quantities. We begin by considering two example form factors, in the orthogonal basis of Section 2.3: $\widetilde{F}_1^{(1)}$ and $\widetilde{F}_{16}^{(1)}$, renormalized and infrared-subtracted according to Eq. (15). In Fig. 6 we show their real and imaginary parts as functions of $\sqrt{s}$. Similar plots for the full set of 18 form factors can be found in Appendix C. The plots contain curves which show the large-m_t expansion (to order $1/m_t^{12}$) and the high-energy expansion (to order $m_t^{30} m_Z^4$ and $m_t^{32} m_Z^4$). Just as at leading order, the high energy expansion does not converge below $\sqrt{s} \approx 750$GeV. The solid curves show the Padé-improved approximations of both the real and imaginary parts of the form factors. In the case of $\widetilde{F}_1^{(1)}$, the plot suggests that for real and imaginary parts the curves merge smoothly into the large-m_t expansion. In the case of $\widetilde{F}_{16}^{(1)}$ we expect a resonance-like structure (as for $F_{16}^{(0)}$ in Fig. 2) which is also indicated by the Padé curves. The thickness of the solid curves reflect our estimate of the uncertainty due to the approximation procedure, as defined in Eq. (37).

Although not the focus of this paper, the form factors also receive contributions from massless quarks running in the loop. We extend the notation of Section 2 and define

$$\overline{F}_i^{(0)} = \sum_{f=u,d,s,c,b} \left(F_{i,\text{ml,box}}^{(0),v_f} + F_{i,\text{ml,box}}^{(0),a_f} \right) + F_i^{(0)} , \qquad (39)$$

where for up-type quarks v_f and a_f are as given in Eq. (6) and for down-type quarks they are given by

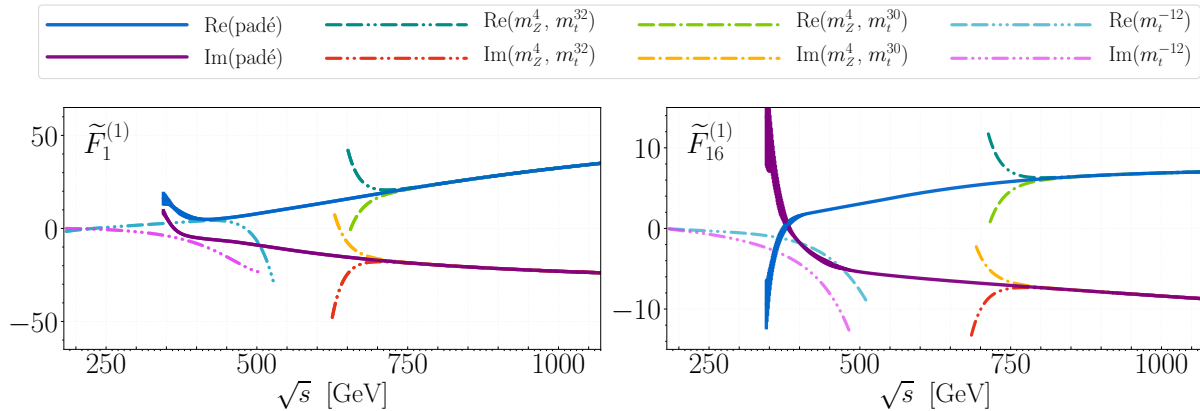$$v_b = -\frac{1}{2} + \frac{2}{3} \sin^2 \theta_W , \qquad a_b = -\frac{1}{2} . \qquad (40)$$

Figure 6: The NLO form factor of the tensor structures T_1 and T_{16} as a function of $\sqrt{s}$, plotted for $\theta = \pi/2$. Both the real and imaginary parts are shown. Dash-dotted and dotted lines correspond to the high-energy and large-m_t results. The solid lines/bands represent the Padé-improved predictions and their uncertainties.

In Eq. (39) $F_i^{(0)}$ corresponds to the LO top quark form factors $f_i^{(0)}$ of Eq. (12), in the orthogonal basis of Section 2.3. There is no contribution from $F_{i,\mathrm{ml,tri}}^{(0)}$ since it is heavily suppressed by the Yukawa couplings of the light quarks and the Higgs boson. We obtain $F_{i,\mathrm{ml,box}}^{(0),v_f}$ and $F_{i,\mathrm{ml,box}}^{(0),a_f}$ by taking the massless limit of the exact LO expressions numerically. Although the NLO massless contributions are known (see Refs. [16, 26]), they are not relevant for our discussion of the quality of the approximations of the NLO top quark-loop contributions. They can be added easily to the final result since they only interfere with the exact LO expressions.

In terms of these $\overline{F}_i^{(0)}$, we now define the finite, virtual contribution to the differential cross section (in analogy to $gg \to HH$ [44, 45]),

$$\widetilde{\mathcal{V}}_{\mathrm{fin}} \;\; = \;\; \frac{\alpha_s^2(\mu)}{\pi^2} \frac{G_F^2 m_Z^4}{32} \sum_{i=1}^{18} \left[C_i + 2 \left(\overline{F}_i^{(0)*} \widetilde{F}_i^{(1)} + \overline{F}_i^{(0)} \widetilde{F}_i^{(1)*} \right) \right] \,, \tag{41}$$

where C_i is defined by

$$C_i \;\; = \;\; \left| \overline{F}_i^{(0)} \right|^2 C_A \left(\pi^2 - \log^2 \frac{\mu^2}{s} \right) . \tag{42}$$

In Eq. (41) α_s corresponds to the five-flavour strong coupling constant. We introduce the quantity

$$\mathcal{V}_{\mathrm{fin}} \;\; = \;\; \frac{\widetilde{\mathcal{V}}_{\mathrm{fin}}}{\alpha_s^2(\mu)} \,, \tag{43}$$

which is discussed in the following. For the renormalization scale we choose $\mu^2 = s/4$.

When evaluating $\mathcal{V}_{\mathrm{fin}}$ we use exact expressions for the LO form factors and our high-energy expansions for the NLO parts. Exact results are known for the two-loop triangle form factors [22–24], however as shown in [35], the high-energy expansions reproduce the exact result almost down to the top threshold, which justifies our use of the expansions to evaluate these contributions also.

In Figs. 7 and 8 we show $\mathcal{V}_{\mathrm{fin}}$ as a function of $\sqrt{s}$ for different values of p_T. In all cases we show Padé-improved results which are obtained by applying the method from Section 4 to $\mathcal{V}_{\mathrm{fin}}$. We start with the numerical evaluation of the form factors $\widetilde{f}_i$, keeping the variable x as introduced in Section 4, perform the basis change to $\widetilde{F}_i$ and then construct $\mathcal{V}_{\mathrm{fin}}$ as an expansion in x. At this point we apply the procedure outlined in Section 4. We take into account the different sets of Padé approximants listed below Eq. (38). Our best prediction, {10,16}, is shown as black points. For higher values of p_T (Fig. 7) we show in addition two curves from the high-energy expansion. For $p_T = 400$ GeV they lie on top of each other and agree with the Padé predictions. For $p_T = 350$ GeV the two high-energy expansion curves differ from each other. The Padé approximations show a stable behaviour, demonstrated by the fact that even with little input ({5,9}) no significant uncertainty is observed.
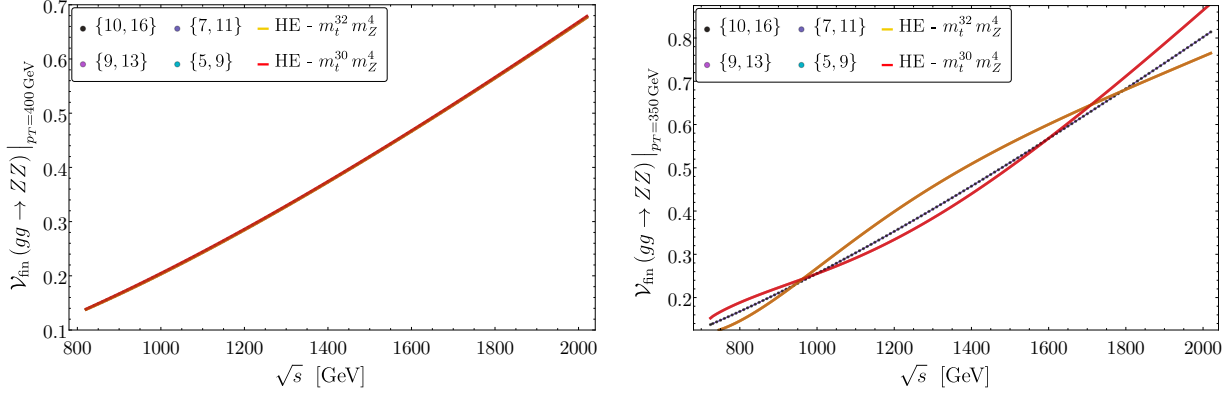
Figure 7: $\mathcal{V}_{\text{fin}}$ as a function of $\sqrt{s}$ for p_T values of 400 and 350 GeV. The curves denoted "HE" show the high-energy expansion to orders $m_t^{30}m_Z^4$ and $m_t^{32}m_Z^4$.
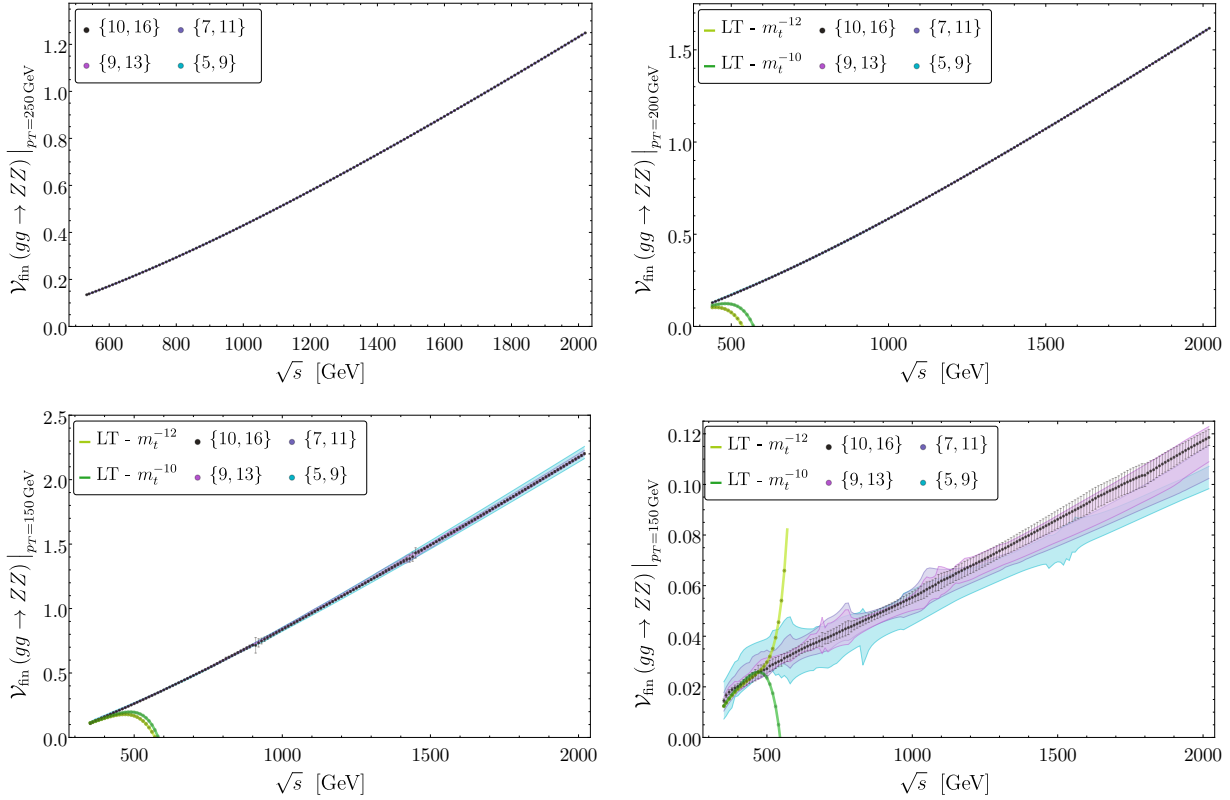

Figure 8: $\mathcal{V}_{\text{fin}}$ as a function of $\sqrt{s}$ for p_T values of 250, 200 and 150 GeV. The curves denoted "LT" show the large-m_t expansion to orders m_t^{-10} and m_t^{-12}. The bottom-right plot excludes the light quark contributions introduced in Eq. (39).

For lower values of p_T (Fig. 8) the high-energy expansion curves lie completely outside of the range of the plot axes. Nonetheless stable Padé predictions are observed, even for

20

the low p_T value of 150 GeV. For this value one observes that the higher orders in the m_t expansion are crucial to obtain estimates with small uncertainties. The bottom-right panel of Fig. 8 shows the same approximations, but excludes the light quark contributions introduced in Eq. (39). This shows in more detail the improvement of the {10,16} approximation with respect to, for example, the {5,9} approximation.

The results presented in Figs. 7 and 8 make predictions for $\mathcal{V}_{\text{fin}}$ which should eventually be confronted with numerical results as, e.g., announced in Ref. [46]. To this end we provide, in the ancillary files of this paper [29], a simple `C++` program which interpolates a pre-evaluated grid of $\mathcal{V}_{\text{fin}}$ points and uncertainties, evaluated with {10,16} for $\mu^2 = s/4$, using routines from the GNU Scientific Library [47]. It can thus be used to reproduce the black points and uncertainty bars of Figs. 7 and 8.

6 Conclusions

We compute NLO QCD corrections to the process $gg \to ZZ$ induced by virtual top quark loops. We concentrate on the high-energy limit which corresponds to an expansion in the parameters m_t^2/s, m_t^2/t and m_t^2/u. We furthermore expand for small Z boson masses and show, at LO, that three expansion terms are sufficient to obtain per-mille accuracy. Analytic results, including terms up to order $m_t^{32}m_Z^4$, are presented for all 20 form factors in the ancillary file [29]. Additionally we include in this file the large-m_t expansions of these 20 form factors, up to order $1/m_t^{12}$.

Using simple tensor structures as a starting point, we construct an orthogonal basis which is convenient when computing the squared amplitude. Alternatively we also provide LO and NLO results for the helicity amplitudes.

We extend the radius of convergence of the high-energy expansions with the help of Padé approximations. Our method provides both a central value and an uncertainty estimate. This is validated by comparisons to known exact results at LO. The Padé method is applied both to the form factors and the NLO virtual corrections to the differential cross section. In the latter case we include in our predictions also the LO contributions which originate from massless quark loops. In this setup the interference of the one- and two-loop top quark contributions amounts to about 5% as can be seen from Fig. 8.

Acknowledgements

A Basis change

In this Appendix we provide the basis change relations from the simple tensor structures $S_i^{\mu\nu\rho\sigma}$ of Eq. (9) to the orthogonal tensors $T_i^{\mu\nu\rho\sigma}$ of Section 2.3. They are given by

$$T_1^{\mu\nu\rho\sigma} = S_{17}^{\mu\nu\rho\sigma} \frac{m_Z^2}{p_T^2 (p_1 \cdot p_3)(p_2 \cdot p_3)} , \tag{44}$$

$$T_2^{\mu\nu\rho\sigma} = S_{17}^{\mu\nu\rho\sigma} \frac{\left(m_Z^2 - p_T^2\right)^2}{4p_T^4 (p_1 \cdot p_3)(p_2 \cdot p_3)} + S_{18}^{\mu\nu\rho\sigma} \frac{\left(m_Z^2 - p_T^2\right)(p_2 \cdot p_3)}{2p_T^4 (p_1 \cdot p_2)(p_1 \cdot p_3)} + S_{19}^{\mu\nu\rho\sigma} \frac{\left(m_Z^2 - p_T^2\right)(p_1 \cdot p_3)}{2p_T^4 (p_1 \cdot p_2)(p_2 \cdot p_3)}$$
$$+ S_{20}^{\mu\nu\rho\sigma} \frac{(p_1 \cdot p_3)(p_2 \cdot p_3)}{p_T^4 (p_1 \cdot p_2)^2} , \tag{45}$$

$$T_3^{\mu\nu\rho\sigma} = S_9^{\mu\nu\rho\sigma} \frac{m_Z^2}{(p_1 \cdot p_3)(p_2 \cdot p_3)} + S_{17}^{\mu\nu\rho\sigma} \frac{m_Z^2}{p_T^2 (p_1 \cdot p_3)(p_2 \cdot p_3)} , \tag{46}$$

$$T_4^{\mu\nu\rho\sigma} = S_9^{\mu\nu\rho\sigma} \frac{\left(m_Z^2 - p_T^2\right)^2}{4p_T^2 (p_1 \cdot p_3)(p_2 \cdot p_3)} + S_{10}^{\mu\nu\rho\sigma} \frac{\left(m_Z^2 - p_T^2\right)(p_2 \cdot p_3)}{2p_T^2 (p_1 \cdot p_2)(p_1 \cdot p_3)} + S_{11}^{\mu\nu\rho\sigma} \frac{\left(m_Z^2 - p_T^2\right)(p_1 \cdot p_3)}{2p_T^2 (p_1 \cdot p_2)(p_2 \cdot p_3)}$$
$$+ S_{12}^{\mu\nu\rho\sigma} \frac{(p_1 \cdot p_3)(p_2 \cdot p_3)}{p_T^2 (p_1 \cdot p_2)^2} + S_{17}^{\mu\nu\rho\sigma} \frac{\left(m_Z^2 - p_T^2\right)^2}{4p_T^4 (p_1 \cdot p_3)(p_2 \cdot p_3)} + S_{18}^{\mu\nu\rho\sigma} \frac{\left(m_Z^2 - p_T^2\right)(p_2 \cdot p_3)}{2p_T^4 (p_1 \cdot p_2)(p_1 \cdot p_3)}$$
$$+ S_{19}^{\mu\nu\rho\sigma} \frac{\left(m_Z^2 - p_T^2\right)(p_1 \cdot p_3)}{2p_T^4 (p_1 \cdot p_2)(p_2 \cdot p_3)} + S_{20}^{\mu\nu\rho\sigma} \frac{(p_1 \cdot p_3)(p_2 \cdot p_3)}{p_T^4 (p_1 \cdot p_2)^2} , \tag{47}$$

$$T_5^{\mu\nu\rho\sigma} = S_4^{\mu\nu\rho\sigma} \frac{\left(m_Z^2 - p_T^2\right)}{2p_T^2 (p_1 \cdot p_3)} + S_5^{\mu\nu\rho\sigma} \frac{(p_1 \cdot p_3)}{p_T^2 (p_1 \cdot p_2)} + S_{17}^{\mu\nu\rho\sigma} \frac{\left(m_Z^2 - p_T^2\right)}{2p_T^4 (p_1 \cdot p_2)} + S_{18}^{\mu\nu\rho\sigma} \frac{\left(m_Z^2 - p_T^2\right)(p_2 \cdot p_3)}{2p_T^4 (p_1 \cdot p_2)(p_1 \cdot p_3)}$$
$$+ S_{19}^{\mu\nu\rho\sigma} \frac{(p_1 \cdot p_3)^2}{p_T^4 (p_1 \cdot p_2)^2} + S_{20}^{\mu\nu\rho\sigma} \frac{(p_1 \cdot p_3)(p_2 \cdot p_3)}{p_T^4 (p_1 \cdot p_2)^2} , \tag{48}$$

$$T_6^{\mu\nu\rho\sigma} = S_{13}^{\mu\nu\rho\sigma} \frac{\left(m_Z^2 - p_T^2\right)}{2p_T^2 (p_2 \cdot p_3)} + S_{14}^{\mu\nu\rho\sigma} \frac{(p_2 \cdot p_3)}{p_T^2 (p_1 \cdot p_2)} - S_{17}^{\mu\nu\rho\sigma} \frac{\left(m_Z^2 - p_T^2\right)}{2p_T^4 (p_1 \cdot p_2)} - S_{18}^{\mu\nu\rho\sigma} \frac{(p_2 \cdot p_3)^2}{p_T^4 (p_1 \cdot p_2)^2}$$
$$- S_{19}^{\mu\nu\rho\sigma} \frac{\left(m_Z^2 - p_T^2\right)(p_1 \cdot p_3)}{2p_T^4 (p_1 \cdot p_2)(p_2 \cdot p_3)} - S_{20}^{\mu\nu\rho\sigma} \frac{(p_1 \cdot p_3)(p_2 \cdot p_3)}{p_T^4 (p_1 \cdot p_2)^2} , \tag{49}$$

$$T_7^{\mu\nu\rho\sigma} = S_6^{\mu\nu\rho\sigma} \frac{(p_2 \cdot p_3)}{p_T^2 (p_1 \cdot p_2)} + S_7^{\mu\nu\rho\sigma} \frac{\left(m_Z^2 - p_T^2\right)}{2p_T^2 (p_2 \cdot p_3)} + S_{17}^{\mu\nu\rho\sigma} \frac{(p_1 \cdot p_3)(p_2 \cdot p_3)}{p_T^4 (p_1 \cdot p_2)^2} + S_{18}^{\mu\nu\rho\sigma} \frac{(p_2 \cdot p_3)^2}{p_T^4 (p_1 \cdot p_2)^2}$$
$$+ S_{19}^{\mu\nu\rho\sigma} \frac{\left(m_Z^2 - p_T^2\right)(p_1 \cdot p_3)}{2p_T^4 (p_1 \cdot p_2)(p_2 \cdot p_3)} + S_{20}^{\mu\nu\rho\sigma} \frac{\left(m_Z^2 - p_T^2\right)}{2p_T^4 (p_1 \cdot p_2)} , \tag{50}$$

$$T_8^{\mu\nu\rho\sigma} = S_{15}^{\mu\nu\rho\sigma} \frac{(p_1 \cdot p_3)}{p_T^2 (p_1 \cdot p_2)} + S_{16}^{\mu\nu\rho\sigma} \frac{\left(m_Z^2 - p_T^2\right)}{2p_T^2 (p_1 \cdot p_3)} + S_{17}^{\mu\nu\rho\sigma} \frac{(p_1 \cdot p_3)(p_2 \cdot p_3)}{p_T^4 (p_1 \cdot p_2)^2} - S_{18}^{\mu\nu\rho\sigma} \frac{\left(m_Z^2 - p_T^2\right)(p_2 \cdot p_3)}{2p_T^4 (p_1 \cdot p_2)(p_1 \cdot p_3)}$$
$$- S_{19}^{\mu\nu\rho\sigma} \frac{(p_1 \cdot p_3)^2}{p_T^4 (p_1 \cdot p_2)^2} - S_{20}^{\mu\nu\rho\sigma} \frac{\left(m_Z^2 - p_T^2\right)}{2p_T^4 (p_1 \cdot p_2)} , \tag{51}$$

$$T_9^{\mu\nu\rho\sigma} = S_8^{\mu\nu\rho\sigma} \frac{1}{p_T^2} - S_{17}^{\mu\nu\rho\sigma} \frac{(p_1 \cdot p_3)(p_2 \cdot p_3)}{p_T^4 (p_1 \cdot p_2)^2} - S_{18}^{\mu\nu\rho\sigma} \frac{p_T^2 (p_1 \cdot p_2) + (p_2 \cdot p_3)^2}{p_T^4 (p_1 \cdot p_2)^2}$$
$$- S_{19}^{\mu\nu\rho\sigma} \frac{p_T^2 (p_1 \cdot p_2) + (p_1 \cdot p_3)^2}{p_T^4 (p_1 \cdot p_2)^2} - S_{20}^{\mu\nu\rho\sigma} \frac{(p_1 \cdot p_3)(p_2 \cdot p_3)}{p_T^4 (p_1 \cdot p_2)^2} , \tag{52}$$

$$T_{10}^{\mu\nu\rho\sigma} = S_3^{\mu\nu\rho\sigma} - S_4^{\mu\nu\rho\sigma} \frac{(p_2 \cdot p_3)}{p_T^2 (p_1 \cdot p_2)} - S_5^{\mu\nu\rho\sigma} \frac{(p_1 \cdot p_3)}{p_T^2 (p_1 \cdot p_2)} + S_{15}^{\mu\nu\rho\sigma} \frac{(p_1 \cdot p_3)}{p_T^2 (p_1 \cdot p_2)} + S_{16}^{\mu\nu\rho\sigma} \frac{(p_2 \cdot p_3)}{p_T^2 (p_1 \cdot p_2)}$$
$$- S_{17}^{\mu\nu\rho\sigma} \frac{(p_1 \cdot p_3)(p_2 \cdot p_3)}{p_T^4 (p_1 \cdot p_2)^2} - S_{18}^{\mu\nu\rho\sigma} \frac{(p_2 \cdot p_3)^2}{p_T^4 (p_1 \cdot p_2)^2} - S_{19}^{\mu\nu\rho\sigma} \frac{(p_1 \cdot p_3)^2}{p_T^4 (p_1 \cdot p_2)^2} - S_{20}^{\mu\nu\rho\sigma} \frac{(p_1 \cdot p_3)(p_2 \cdot p_3)}{p_T^4 (p_1 \cdot p_2)^2} , \tag{53}$$

$$T_{11}^{\mu\nu\rho\sigma} = S_{17}^{\mu\nu\rho\sigma} \frac{m_Z^2 \left(m_Z^2 - p_T^2\right)}{2p_T^2 (p_1 \cdot p_3)(p_2 \cdot p_3)} + S_{19}^{\mu\nu\rho\sigma} \frac{m_Z^2 (p_1 \cdot p_3)}{p_T^2 (p_1 \cdot p_2)(p_2 \cdot p_3)} \,, \tag{54}$$

$$T_{12}^{\mu\nu\rho\sigma} = S_{17}^{\mu\nu\rho\sigma} \frac{m_Z^2 \left(m_Z^2 - p_T^2\right)}{2p_T^2 (p_1 \cdot p_3)(p_2 \cdot p_3)} + S_{18}^{\mu\nu\rho\sigma} \frac{m_Z^2 (p_2 \cdot p_3)}{p_T^2 (p_1 \cdot p_2)(p_1 \cdot p_3)} \,, \tag{55}$$

$$T_{13}^{\mu\nu\rho\sigma} = S_{7}^{\mu\nu\rho\sigma} \frac{m_Z^2}{(p_2 \cdot p_3)} + S_{19}^{\mu\nu\rho\sigma} \frac{m_Z^2 (p_1 \cdot p_3)}{p_T^2 (p_1 \cdot p_2)(p_2 \cdot p_3)} + S_{20}^{\mu\nu\rho\sigma} \frac{m_Z^2}{p_T^2 (p_1 \cdot p_2)} \,, \tag{56}$$

$$T_{14}^{\mu\nu\rho\sigma} = S_{16}^{\mu\nu\rho\sigma} \frac{m_Z^2}{(p_1 \cdot p_3)} - S_{18}^{\mu\nu\rho\sigma} \frac{m_Z^2 (p_2 \cdot p_3)}{p_T^2 (p_1 \cdot p_2)(p_1 \cdot p_3)} - S_{20}^{\mu\nu\rho\sigma} \frac{m_Z^2}{p_T^2 (p_1 \cdot p_2)} \,, \tag{57}$$

$$T_{15}^{\mu\nu\rho\sigma} = + S_{4}^{\mu\nu\rho\sigma} \frac{m_Z^2}{(p_1 \cdot p_3)} + S_{18}^{\mu\nu\rho\sigma} \frac{m_Z^2 (p_2 \cdot p_3)}{p_T^2 (p_1 \cdot p_2)(p_1 \cdot p_3)} + S_{17}^{\mu\nu\rho\sigma} \frac{m_Z^2}{p_T^2 (p_1 \cdot p_2)} \,, \tag{58}$$

$$T_{16}^{\mu\nu\rho\sigma} = S_{13}^{\mu\nu\rho\sigma} \frac{m_Z^2}{(p_2 \cdot p_3)} - S_{17}^{\mu\nu\rho\sigma} \frac{m_Z^2}{p_T^2 (p_1 \cdot p_2)} - S_{19}^{\mu\nu\rho\sigma} \frac{m_Z^2 (p_1 \cdot p_3)}{p_T^2 (p_1 \cdot p_2)(p_2 \cdot p_3)} \,, \tag{59}$$

$$T_{17}^{\mu\nu\rho\sigma} = S_{9}^{\mu\nu\rho\sigma} \frac{m_Z^2 \left(m_Z^2 - p_T^2\right)}{2(p_1 \cdot p_3)(p_2 \cdot p_3)} + S_{11}^{\mu\nu\rho\sigma} \frac{m_Z^2 (p_1 \cdot p_3)}{(p_1 \cdot p_2)(p_2 \cdot p_3)} + S_{17}^{\mu\nu\rho\sigma} \frac{m_Z^2 \left(m_Z^2 - p_T^2\right)}{2p_T^2 (p_1 \cdot p_3)(p_2 \cdot p_3)}$$
$$+ S_{19}^{\mu\nu\rho\sigma} \frac{m_Z^2 (p_1 \cdot p_3)}{p_T^2 (p_1 \cdot p_2)(p_2 \cdot p_3)} \,, \tag{60}$$

$$T_{18}^{\mu\nu\rho\sigma} = S_{9}^{\mu\nu\rho\sigma} \frac{m_Z^2 \left(m_Z^2 - p_T^2\right)}{2(p_1 \cdot p_3)(p_2 \cdot p_3)} + S_{10}^{\mu\nu\rho\sigma} \frac{m_Z^2 (p_2 \cdot p_3)}{(p_1 \cdot p_2)(p_1 \cdot p_3)} + S_{17}^{\mu\nu\rho\sigma} \frac{m_Z^2 \left(m_Z^2 - p_T^2\right)}{2p_T^2 (p_1 \cdot p_3)(p_2 \cdot p_3)}$$
$$+ S_{18}^{\mu\nu\rho\sigma} \frac{m_Z^2 (p_2 \cdot p_3)}{p_T^2 (p_1 \cdot p_2)(p_1 \cdot p_3)} \,, \tag{61}$$

$$T_{19}^{\mu\nu\rho\sigma} = S_{2}^{\mu\nu\rho\sigma} - S_{3}^{\mu\nu\rho\sigma} + S_{4}^{\mu\nu\rho\sigma} \frac{(p_2 \cdot p_3)}{p_T^2 (p_1 \cdot p_2)} + S_{5}^{\mu\nu\rho\sigma} \frac{(p_1 \cdot p_3)}{p_T^2 (p_1 \cdot p_2)} - S_{6}^{\mu\nu\rho\sigma} \frac{(p_2 \cdot p_3)}{p_T^2 (p_1 \cdot p_2)}$$
$$- S_{7}^{\mu\nu\rho\sigma} \frac{(p_1 \cdot p_3)}{p_T^2 (p_1 \cdot p_2)} + S_{13}^{\mu\nu\rho\sigma} \frac{(p_1 \cdot p_3)}{p_T^2 (p_1 \cdot p_2)} + S_{14}^{\mu\nu\rho\sigma} \frac{(p_2 \cdot p_3)}{p_T^2 (p_1 \cdot p_2)} - S_{15}^{\mu\nu\rho\sigma} \frac{(p_1 \cdot p_3)}{p_T^2 (p_1 \cdot p_2)}$$
$$- S_{16}^{\mu\nu\rho\sigma} \frac{(p_2 \cdot p_3)}{p_T^2 (p_1 \cdot p_2)} \,, \tag{62}$$

$$T_{20}^{\mu\nu\rho\sigma} = S_{1}^{\mu\nu\rho\sigma} - S_{3}^{\mu\nu\rho\sigma} + S_{4}^{\mu\nu\rho\sigma} \frac{(p_2 \cdot p_3)}{p_T^2 (p_1 \cdot p_2)} + S_{5}^{\mu\nu\rho\sigma} \frac{(p_1 \cdot p_3)}{p_T^2 (p_1 \cdot p_2)} + S_{8}^{\mu\nu\rho\sigma} \frac{1}{p_T^2}$$
$$- S_{9}^{\mu\nu\rho\sigma} \frac{(p_1 \cdot p_3)(p_2 \cdot p_3)}{p_T^2 (p_1 \cdot p_2)^2} - S_{10}^{\mu\nu\rho\sigma} \frac{p_T^2 (p_1 \cdot p_2) + (p_2 \cdot p_3)^2}{p_T^2 (p_1 \cdot p_2)^2} - S_{11}^{\mu\nu\rho\sigma} \frac{p_T^2 (p_1 \cdot p_2) + (p_1 \cdot p_3)^2}{p_T^2 (p_1 \cdot p_2)^2}$$
$$- S_{12}^{\mu\nu\rho\sigma} \frac{(p_1 \cdot p_3)(p_2 \cdot p_3)}{p_T^2 (p_1 \cdot p_2)^2} - S_{15}^{\mu\nu\rho\sigma} \frac{(p_1 \cdot p_3)}{p_T^2 (p_1 \cdot p_2)} - S_{16}^{\mu\nu\rho\sigma} \frac{(p_2 \cdot p_3)}{p_T^2 (p_1 \cdot p_2)} - S_{18}^{\mu\nu\rho\sigma} \frac{1}{p_T^2 (p_1 \cdot p_2)}$$
$$- S_{19}^{\mu\nu\rho\sigma} \frac{1}{p_T^2 (p_1 \cdot p_2)} \,. \tag{63}$$

These relations, as well as the inverse relations, are available in a computer-readable format in Ref. [29].
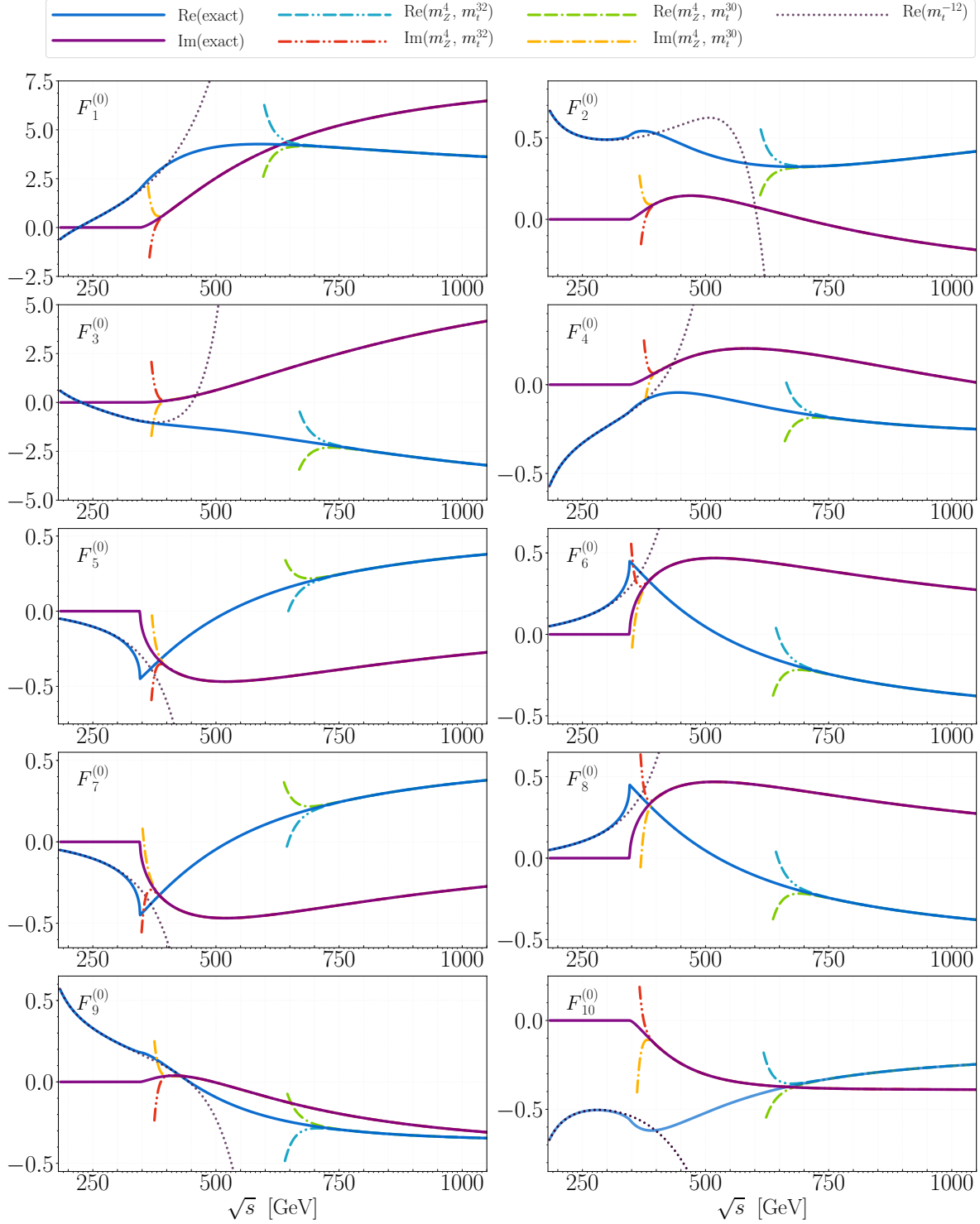
B LO results for form factors

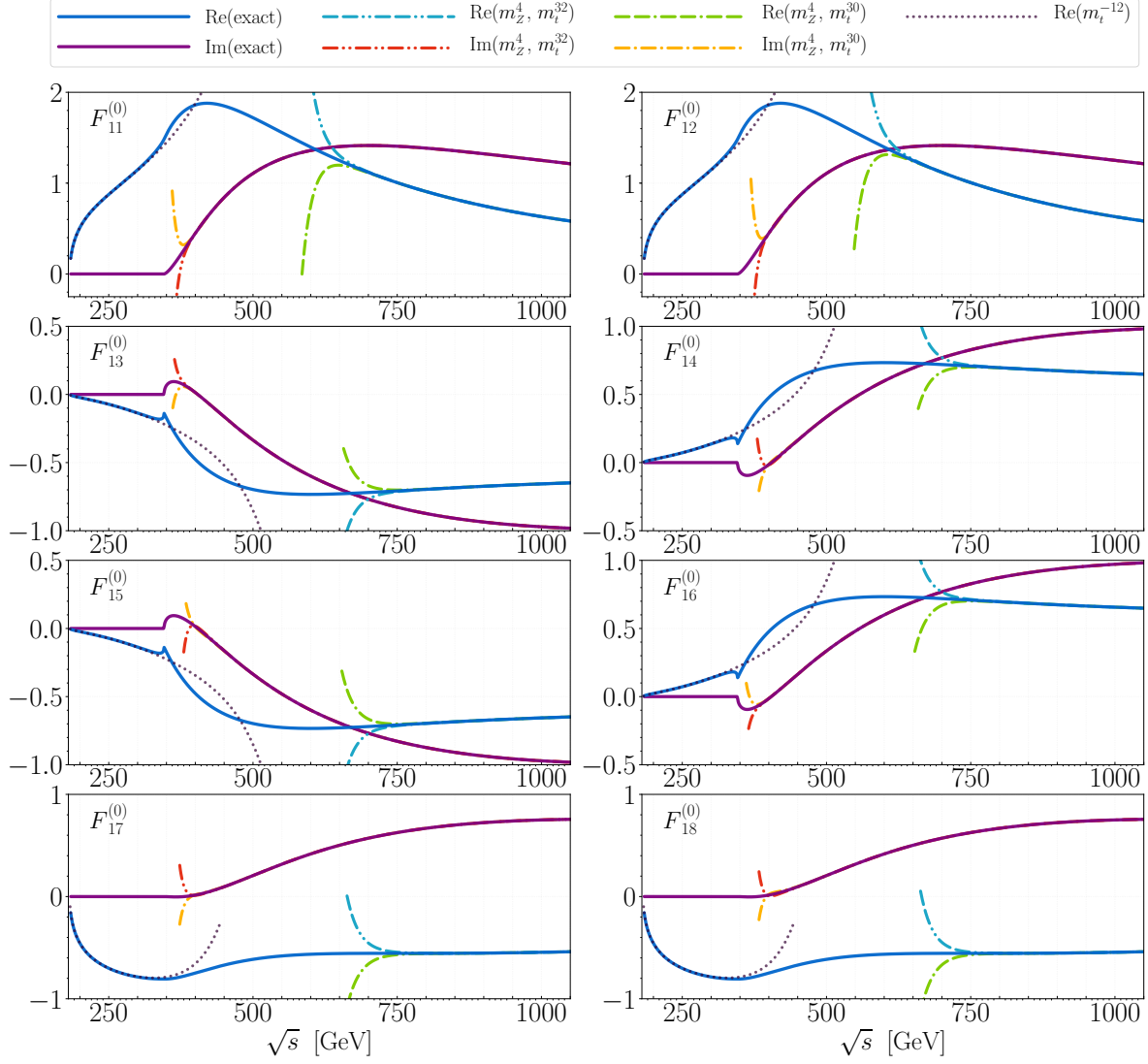Figure 9: $F_1^{(0)}, \ldots, F_{10}^{(0)}$ as a function of $\sqrt{s}$, for $\theta = \pi/2$.

Figure 10: $F_{11}^{(0)}, \ldots, F_{18}^{(0)}$ as a function of $\sqrt{s}$, for $\theta = \pi/2$.
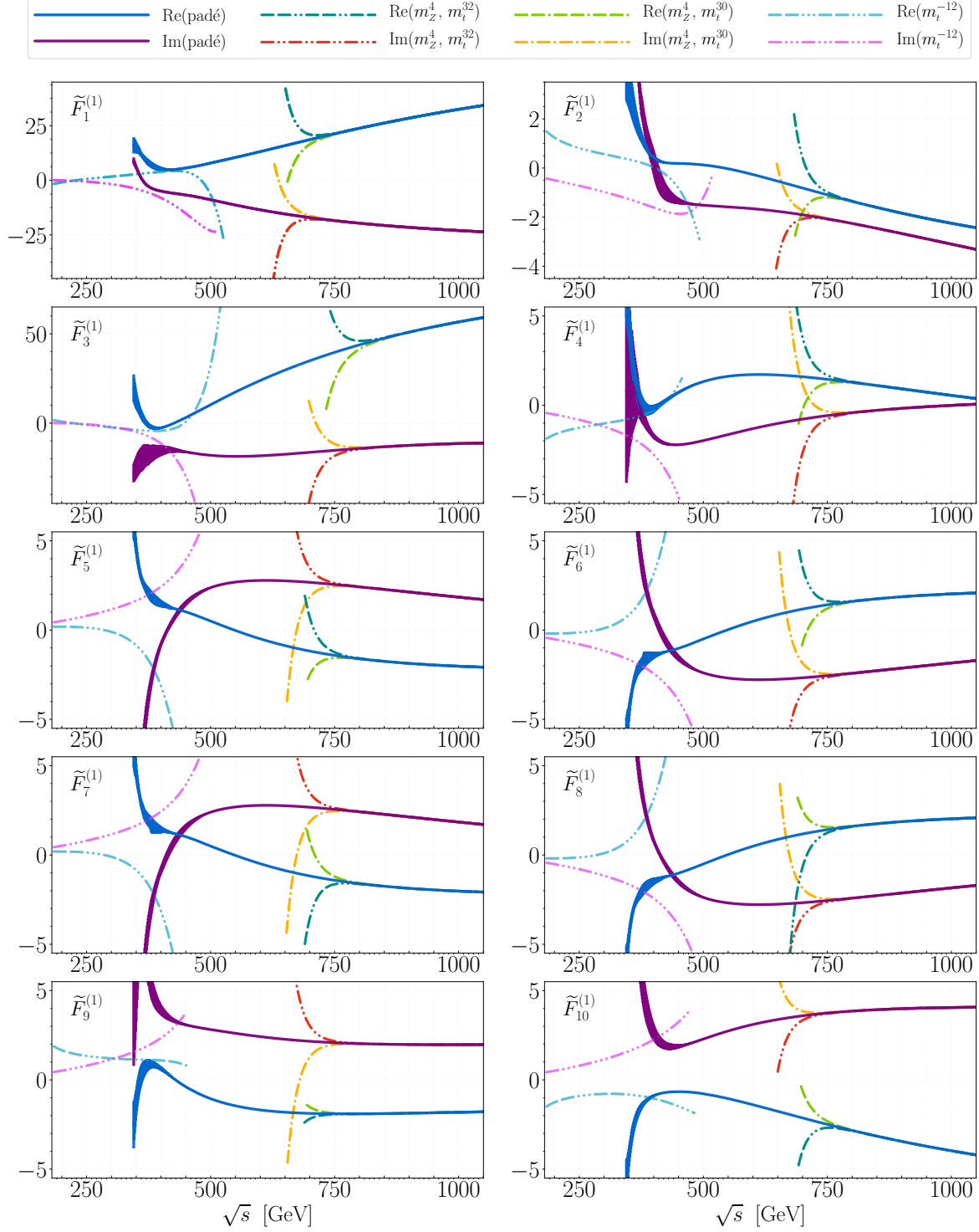
C NLO results for form factors

Figure 11: $\widetilde{F}_1^{(1)}, \ldots, \widetilde{F}_{10}^{(1)}$ as a function of $\sqrt{s}$, for $\theta = \pi/2$.
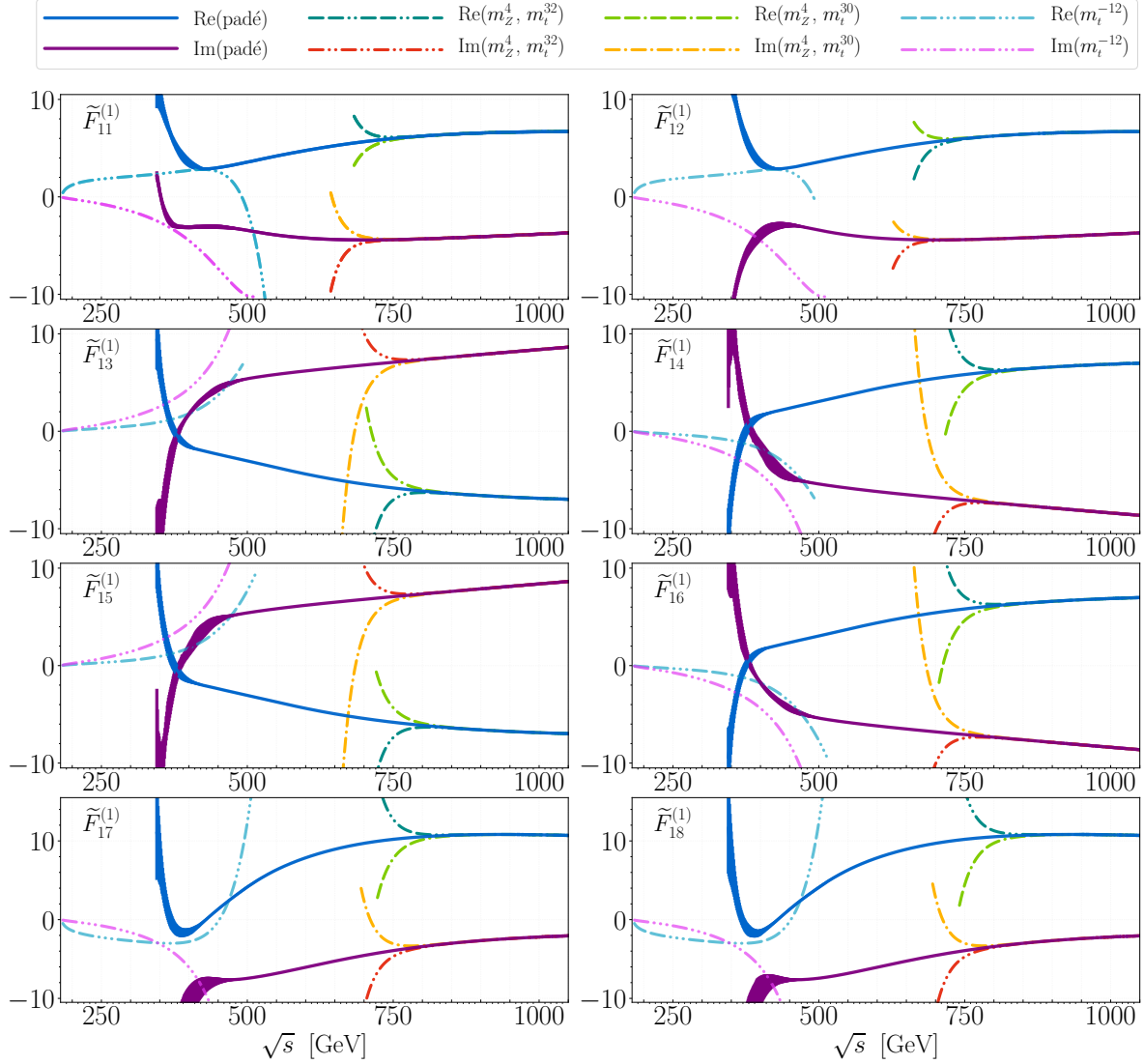
Figure 12: $\widetilde{F}_{11}^{(1)}, \ldots, \widetilde{F}_{18}^{(1)}$ as a function of $\sqrt{s}$, for $\theta = \pi/2$.

D   Example analytic results for LO expansions

In the ancillary file, we provide analytic expressions for the form factors defined in Eq. (12), as expansions in both the large-m_t and high-energy limits. For the convenience of the reader we show here, for LO f_1 and f_3, the leading terms of the expansions in a typeset form. In the large-m_t limit they are given by

$$f_{1,\text{tri}}^{(0)} = -1 + \mathcal{O}\left(\frac{1}{m_t^2}\right),$$

$$f_{1,\text{box}}^{(0),v_t} = v_t^2 \left[\frac{3s^2 - 14st - 14t^2}{360 m_t^4} + \mathcal{O}(m_Z^2)\right] + \mathcal{O}\left(\frac{1}{m_t^6}\right),$$

$$f_{1,\text{box}}^{(0),a_t} = a_t^2 \left[\frac{s}{3m_t^2} + \mathcal{O}(m_Z^2) \right] + \mathcal{O}\left(\frac{1}{m_t^4} \right) ,$$

$$f_{3,\text{box}}^{(0),v_t} = v_t^2 \left[\frac{3s^2 + 20st + 3t^2}{360m_t^4} + \mathcal{O}(m_Z^2) \right] + \mathcal{O}\left(\frac{1}{m_t^6} \right) ,$$

$$f_{3,\text{box}}^{(0),a_t} = a_t^2 \left[-\frac{s}{6m_t^2} + \mathcal{O}(m_Z^2) \right] + \mathcal{O}\left(\frac{1}{m_t^4} \right) . \tag{64}$$

and in the high-energy limit by

$$f_{1,\text{tri}}^{(0)} = m_t^2 \left(\frac{3l_{ms}^2}{2s} - \frac{6}{s} \right) + \mathcal{O}\left(m_t^4 \right) ,$$

$$f_{1,\text{box}}^{(0),v_t} = v_t^2 \left[\frac{l_{1ts}^2(s+t)\left(s^3 + 3s^2 t + t^3\right)}{6s^2 t^2} + \frac{l_{ts} t^2}{3s^2 + 3st} - \frac{l_{ts} l_{1ts}\left(3s^2 + 2st + 2t^2\right)}{6s^2} \right.$$
$$- \frac{1}{3} + \frac{\pi^2 \left(2s^6 + 12s^5 t + 21s^4 t^2 + 20s^3 t^3 + 15s^2 t^4 + 6st^5 + 2t^6\right)}{12s^2 t^2 (s+t)^2}$$
$$\left. - \frac{l_{1ts}(s+t)^2}{3st} + \frac{l_{ts}^2 t\left(3s^3 + 6s^2 t + 3st^2 + t^3\right)}{6s^2 (s+t)^2} + \mathcal{O}\left(m_Z^2 \right) \right] + \mathcal{O}\left(m_t^2 \right) ,$$

$$f_{3,\text{box}}^{(0),v_t} = v_t^2 \left[\frac{l_{1ts}^2 \left(s^4 - 2s^3 t - 3s^2 t^2 - 2st^3 + t^4\right)}{6s^2 t^2} + \frac{l_{ts} l_{1ts}\left(3s^2 + 4st - 2t^2\right)}{6s^2} \right.$$
$$+ \frac{l_{ts} t^2}{3s^2 + 3st} + \frac{1}{3} l_{1ts}\left(-\frac{s}{t} - \frac{t}{s} + 1 \right) + \frac{l_{ts}^2 t\left(-3s^3 - 3s^2 t + t^3\right)}{6s^2 (s+t)^2}$$
$$\left. - \frac{1}{3} + \frac{\pi^2 \left(2s^6 - 9s^4 t^2 - 16s^3 t^3 - 9s^2 t^4 + 2t^6\right)}{12s^2 t^2 (s+t)^2} + \mathcal{O}\left(m_Z^2 \right) \right] + \mathcal{O}\left(m_t^2 \right) , \tag{65}$$

where $l_{ms} = \log\left(m_t^2/s\right) + i\pi$, $l_{ts} = \log\left(-t/s\right) + i\pi$ and $l_{1ts} = \log\left(1 + t/s\right) + i\pi$. Here we show only $f_{1,\text{box}}^{(0),v_t}$ and $f_{3,\text{box}}^{(0),v_t}$ since, for the leading terms, they are equal to $f_{1,\text{box}}^{(0),a_t}$ and $f_{3,\text{box}}^{(0),a_t}$ up to the replacement $v_t^2 \to a_t^2$ as explained below Eq. (12).

References

[1] M. Aaboud *et al.* [ATLAS Collaboration], JHEP **1910** (2019) 127 [arXiv:1905.07163 [hep-ex]].

[2] A. M. Sirunyan *et al.* [CMS Collaboration], Eur. Phys. J. C **78** (2018) 165 Erratum: [Eur. Phys. J. C **78** (2018) no.6, 515] [arXiv:1709.08601 [hep-ex]].

[3] M. Aaboud *et al.* [ATLAS Collaboration], Phys. Lett. B **786** (2018) 223 [arXiv:1808.01191 [hep-ex]].

[4] A. M. Sirunyan *et al.* [CMS Collaboration], Phys. Rev. D **99** (2019) no.11, 112003 [arXiv:1901.00174 [hep-ex]].

[5] N. Kauer and G. Passarino, JHEP **1208** (2012) 116 [arXiv:1206.4803 [hep-ph]].

[6] F. Caola and K. Melnikov, Phys. Rev. D **88** (2013) 054024 [arXiv:1307.4935 [hep-ph]].

[7] J. M. Campbell, R. K. Ellis and C. Williams, JHEP **1404** (2014) 060 [arXiv:1311.3589 [hep-ph]].

[8] F. Cascioli *et al.*, Phys. Lett. B **735** (2014) 311 [arXiv:1405.2219 [hep-ph]].

[9] G. Heinrich, S. Jahn, S. P. Jones, M. Kerner and J. Pires, JHEP **1803** (2018) 142 [arXiv:1710.06294 [hep-ph]].

[10] T. Gehrmann, A. von Manteuffel, L. Tancredi and E. Weihs, JHEP **1406** (2014) 032 [arXiv:1404.4853 [hep-ph]].

[11] F. Caola, J. M. Henn, K. Melnikov, A. V. Smirnov and V. A. Smirnov, JHEP **1411** (2014) 041 [arXiv:1408.6409 [hep-ph]].

[12] T. Gehrmann, A. von Manteuffel and L. Tancredi, JHEP **1509** (2015) 128 [arXiv:1503.04812 [hep-ph]].

[13] M. Grazzini, S. Kallweit and D. Rathlev, Phys. Lett. B **750** (2015) 407 [arXiv:1507.06257 [hep-ph]].

[14] S. Kallweit and M. Wiesemann, Phys. Lett. B **786** (2018) 382 [arXiv:1806.05941 [hep-ph]].

[15] E. W. N. Glover and J. J. van der Bij, Nucl. Phys. B **321** (1989) 561.

[16] A. von Manteuffel and L. Tancredi, JHEP **1506** (2015) 197 [arXiv:1503.08835 [hep-ph]].

[17] F. Caola, K. Melnikov, R. Rntsch and L. Tancredi, Phys. Rev. D **92** (2015) no.9, 094028 [arXiv:1509.06734 [hep-ph]].

[18] M. Grazzini, S. Kallweit, M. Wiesemann and J. Y. Yook, JHEP **1903** (2019) 070 [arXiv:1811.09593 [hep-ph]].

[19] K. Melnikov and M. Dowling, Phys. Lett. B **744** (2015) 43 [arXiv:1503.01274 [hep-ph]].

[20] J. M. Campbell, R. K. Ellis, M. Czakon and S. Kirchner, JHEP **1608** (2016) 011 [arXiv:1605.01380 [hep-ph]].

[21] R. Gröber, A. Maier and T. Rauh, arXiv:1908.04061 [hep-ph].

[22] R. Harlander and P. Kant, JHEP **0512** (2005) 015 [hep-ph/0509189].

[23] C. Anastasiou, S. Beerli, S. Bucherer, A. Daleo and Z. Kunszt, JHEP **0701** (2007) 082 [hep-ph/0611236].

[24] U. Aglietti, R. Bonciani, G. Degrassi and A. Vicini, JHEP **0701** (2007) 021 [hep-ph/0611266].

[25] L. J. Dixon, arXiv:1310.5353 [hep-ph].

[26] F. Caola, J. M. Henn, K. Melnikov, A. V. Smirnov and V. A. Smirnov, JHEP **1506** (2015) 129 [arXiv:1503.08759 [hep-ph]].

[27] D. Wellmann, "Top Quark Mass Effects in Higgs and Z Boson Pair Production and Higgs Boson Decays", PhD thesis, KIT, 2020.

[28] S. Catani, Phys. Lett. B **427** (1998) 161 [hep-ph/9802439].

[29] https://www.ttp.kit.edu/preprints/2020/ttp20-006/.

[30] P. Nogueira, J. Comput. Phys. **105** (1993) 279.

[31] T. Hahn, Comput. Phys. Commun. **140** (2001) 418 [hep-ph/0012260].

[32] T. Hahn, S. Paehr and C. Schappacher, PoS LL **2016** (2016) 068 [J. Phys. Conf. Ser. **762** (2016) no.1, 012065] [arXiv:1604.04611 [hep-ph]].

[33] H. H. Patel, Comput. Phys. Commun. **218** (2017) 66 [arXiv:1612.00009 [hep-ph]].

[34] J. Davies, G. Mishima, M. Steinhauser and D. Wellmann, JHEP **1803** (2018) 048 [arXiv:1801.09696 [hep-ph]].

[35] J. Davies, G. Mishima, M. Steinhauser and D. Wellmann, JHEP **1901** (2019) 176 [arXiv:1811.05489 [hep-ph]].

[36] R. N. Lee, J. Phys. Conf. Ser. **523** (2014) 012059 [arXiv:1310.1145 [hep-ph]].

[37] B. Ruijl, T. Ueda and J. Vermaseren, arXiv:1707.06453 [hep-ph].

[38] A. V. Smirnov and F. S. Chuharev, arXiv:1901.07808 [hep-ph].

[39] D. Maitre, Comput. Phys. Commun. **183** (2012) 846 [hep-ph/0703052].

[40] J. Grigo, J. Hoff, K. Melnikov and M. Steinhauser, Nucl. Phys. B **875** (2013) 1 [arXiv:1305.7340 [hep-ph]].

[41] R. Harlander, T. Seidensticker and M. Steinhauser, Phys. Lett. B **426** (1998) 125 [hep-ph/9712228].

[42] T. Seidensticker, hep-ph/9905298.

[43] M. Tanabashi *et al.* [Particle Data Group], Phys. Rev. D **98** (2018) no.3, 030001.

[44] J. Davies, G. Heinrich, S. P. Jones, M. Kerner, G. Mishima, M. Steinhauser and D. Wellmann, JHEP **1911** (2019) 024 [arXiv:1907.06408 [hep-ph]].

[45] G. Heinrich, S. P. Jones, M. Kerner, G. Luisoni and E. Vryonidou, JHEP **1708** (2017) 088 [arXiv:1703.09252 [hep-ph]].

[46] B. Agarwal and A. Von Manteuffel, arXiv:1912.08794 [hep-ph].

[47] M. Galassi et al, GNU Scientific Library Reference Manual (3rd Ed.), ISBN 0954612078.